Detection of Anthropogenic CO_2 Emissions Sources (DACES)

Final report

Author: Iolanda Ialongo and Janne Hakkarainen
Institute: Finnish Meteorological Institute, Helsinki, Finland

Version: 1.1
Date: 8 June 2020

Project: “Detection of Anthropogenic CO_2 Emissions Sources (DACES)”

ESA EO Science 4 Society
Activity line: Scientific Data Exploitation

Context

1 Introduction

Anthropogenic emissions from fossil fuel combustion have large impacts on climate. The Paris Agreement emphasizes the need to monitor the CO2 concentrations in the atmosphere to support climate change mitigation actions. Satellite CO2 observations offer the opportunity to monitor the CO2 levels on global scale. Current CO2 missions have been primarily designed to extend the spatial coverage of the ground-based atmospheric observation networks and to improve the model estimates of biospheric fluxes on regional scale.

Recently, direct methods, i.e. the methods that do not involve atmospheric inverse modeling, have been developed to study anthropogenic CO2 emissions. These methods can be divided in two categories a) methods that study anthropogenic sources from individual orbits (e.g., Nassar et al., 2017; Schwandner et al, 2017); and b) methods that average data from long period of time (e.g., Hakkarainen et al., 2016). DACES project explores both these approaches for monitoring anthropogenic CO2 signatures from global to local scale, including an assessment on the methods to derive emission estimates.

In addition to GHGs, short-lived pollutants (such as NO2 and SO2) are also measured from space. Satellite instruments like the Ozone Monitoring Instrument, OMI (and very recently TROPOMI/S5P), have been providing accurate information about the spatio-temporal distribution of such pollutants in the atmosphere and on their emission sources. The synergy between space-based measurements GHG and short-lived gases is expected to provide new insights in understanding the anthropogenic contribution to the CO2 levels in the atmosphere.

The DACES project developed new methodologies for detecting anthropogenic carbon dioxide (CO2) emission sources using satellite-based observations. These approaches are based on the synergy between satellite observations of CO2 (mainly from NASA's OCO-2 instrument) and short-lived gases (e.g. TROPOMI NO2 and SO2 products). Also, DACES project focused on evaluating of potential of satellite-based atmospheric observations for societal applications and user engagement. The results achieved within the DACES project provide useful tools to analyze observations from future CO2 satellite missions, such as the anthropogenic CO2 monitoring mission planned by the European Space Agency.

In this report, we present the main results achieved in the DACES project. In section 2 we present the scientific results, including the analysis of the global XCO2 anomalies and the local plume detection method and examples. In section 3 we discuss several user cases in which satellite atmospheric observations have been applied to monitor anthropogenic emission changes in support of decision makers and sustainable development actions. Section 4 includes the description of the outreach activities such as scientific meeting and publications, and communication to the public. Finally, section 5 includes the discussion of the results and future plans.

2 Scientific results

2.1 Global XCO2 anomalies

2.1.1 Datasets

We use CO2 data from NASA's OCO-2 satellite (Crisp et al., 2017). The satellite was launched on 2 July 2014, and now leads the 705 km Afternoon Constellation, A-Train. OCO-2 has provided science data since September 2014. The instrument measures the backscattered solar light in three spectral regions: oxygen A-band at 0.765 microns and CO2 bands at 1.61 and 2.06 microns. It provides data with eight 2.25 km long footprints along a narrow swath (<10 km). The retrieved quantity is column-averaged dry air mole fraction of CO2, XCO2. We use the latest OCO-2 data version (V9r) available from the MIRADOR platform at http://mirador.gsfc.nasa.gov, but we also compare to earlier versions, namely V7r and V8r. We use the lite files that include bias correction and data screening as well as quality flags set to zero. The validation of OCO-2 data indicates that the absolute median differences are less than 0.4 ppm and the RMS differences are less than 1.5 ppm (Wunch et al., 2017).

The TROPOspheric Monitoring Instrument (TROPOMI) is the instrument on board of the Copernicus Sentinel-5 Precursor satellite, launched on October 13th, 2017. TROPOMI is a nadir viewing spectrometer operating in the UV-VIS (270-495 nm), the near IR (675- 775 nm) and the shortwave IR (2305-2385 nm). TROPOMI provides daily global coverage with a spatial resolution of 3.5 km ×7 km in nadir direction (NO2, 7 km ×7 km for CO). TROPOMI observes NO2, SO2 and CO, among other atmospheric parameters. For more information on the algorithms see the TROPOMI special issue: https://www.atmos-meas-tech.net/special_issue80.html

For meteorological data we use data from ECMWF ERA5 reanalysis data. In our analysis we mainly use 10m u and v wind components.

2.1.2 Methodology

CO2 has a long atmospheric lifetime and relatively large background concentrations (~410 ppm). Because of this, XCO2 varies by only about 2% from pole-to-pole and over the seasonal cycle. Meanwhile, XCO2 variations corresponding to anthropogenic sources are even smaller on the scale of the satellite sounding (2–4 km^2). High precision is therefore essential to quantify XCO2 anomalies associated with these sources. Methods like those used to map short-lived air pollutants, like NO2, based on averaging out the outflow downwind from the emission sources, cannot be directly applied to space-based CO2 measurements. The large CO2 background and seasonal variability must be removed before being able to highlight the emission areas.

In order to extract information about the anthropogenic and biogenic signatures from OCO-2 retrievals, we use the concept of XCO2 anomaly (Hakkarainen et al., 2016), defined as the difference between the individual XCO2 value measured by OCO-2 and the daily background:

XCO2(anomaly) = XCO2(individual) – XCO2(daily background).

This equation provides an anomaly value for each OCO-2 data point. Using the daily background allows us to remove the seasonal variability and the increasing trend of CO2 concentrations. Once we obtain the anomalies for each OCO-2 measurement point, we define a spatial grid (e.g., 1°× 1°, latitude-longitude) and calculate the mean at each grid point over a defined period of time. Figure 1 shows examples of mean XCO2 anomalies for one day, one week, one month and one year. The resulting anomaly maps illustrate the areas where CO2 is emitted (positive anomalies) into the atmosphere and those acting as sinks, where CO2 is absorbed at the surface (negative anomalies). The strength of this approach is that it only uses satellite-based measurements and is not dependent on patterns in a priori fields, external data or other assumptions in atmospheric chemistry-transport models.

Defining the area, over which the daily background is calculated, is a critical step in the analysis. In Hakkarainen et al. (2016), we focused on three selected anthropogenic emission areas: (1) North America, (2) Europe, northern Africa, and Middle East, and (3) East Asia. When analyzing local case studies on regional scales, a different background region can be selected, as shown for example in the South Africa's case study showed later in this report or by Wang et al. (2018) in China. Here our aim is to obtain comparable anomalies for different regions. In order to obtain the background, we calculate the daily medians for each 10-degree latitude band and linearly interpolate the resulting values to each OCO-2 data point. The median was chosen because it better represents the typical value in each latitude band, and it is not skewed towards extreme values.

Figure 2 show daily medians for different 20-degree latitude bands. We can observe the CO2 seasonal cycle (stronger in the Northern Hemisphere) and the increasing trend. We noted that using a hemispheric background or narrow latitude bands without interpolation, will yield to sharp latitudinal boundaries in the maps as observed from Figure 3. In particular, the sharpest boundary is visible between the northern high mid-latitudes (40°N–60°N) and lower latitudes during summer months due to the stronger (and shifted) CO2 uptake.

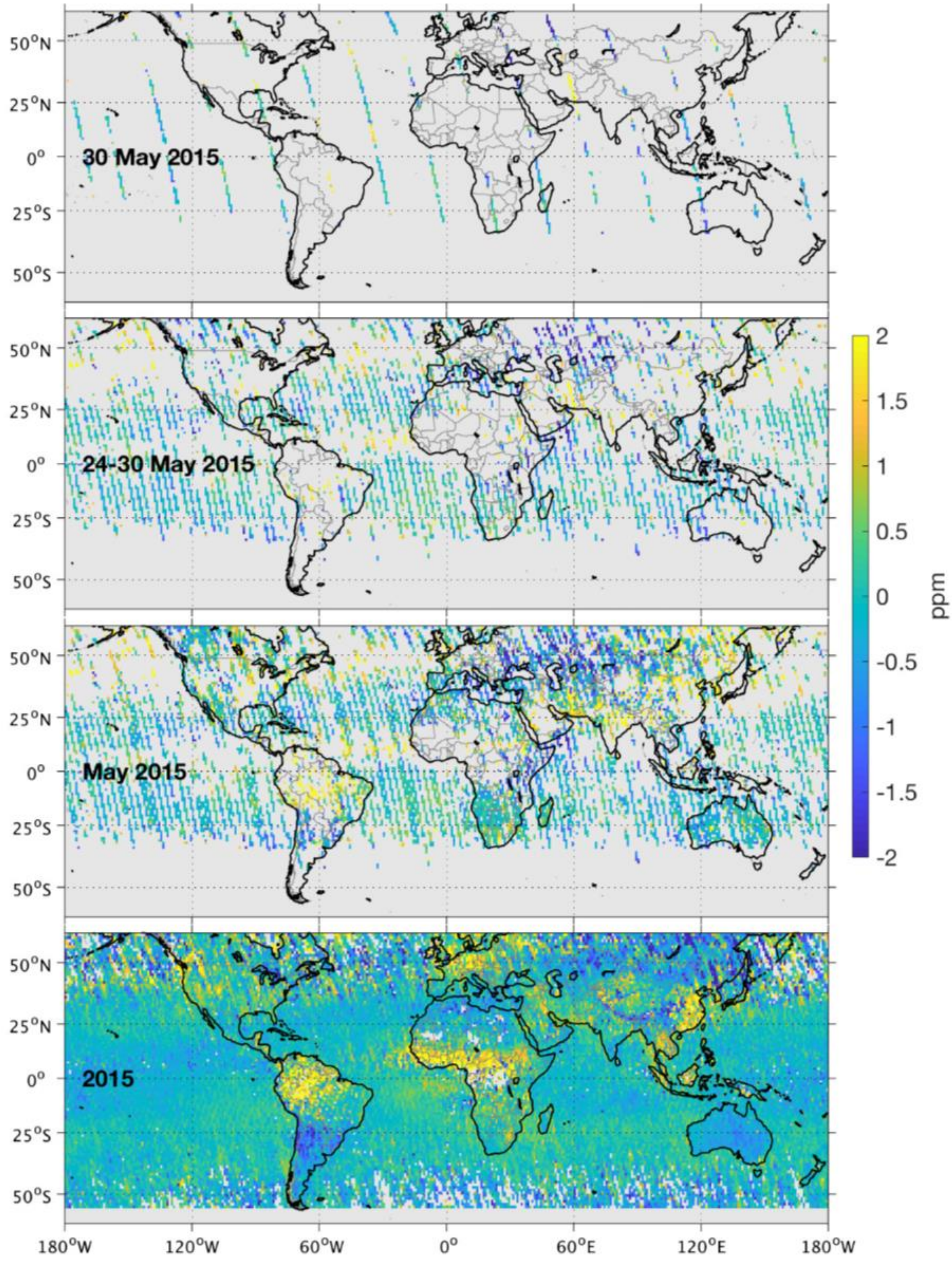

Figure 1 Mean Orbiting Carbon Observatory-2 (OCO-2) XCO2 anomalies on 1°× 1° latitude-longitude grid during one day, one week, one month and one year. For the background we calculate the daily medians for each 10-degree latitude bands and linearly interpolate the resulting values to each OCO-2 data point.

Figure 4 shows the daily XCO2 background as a function of latitude interpolated at 1-degree resolution. The interpolation step removes the sharp latitudinal boundaries that would result if the daily medians at different latitude bands were used directly. The background used in the calculation of the anomalies changes at different times of the year and over different regions. The peak of the seasonal cycle shifts during the year from the Northern to the Southern hemisphere. Also the amplitude of the seasonal cycle is much larger in the Northern Hemisphere due to the strong seasonal biospheric flux differences. Figure 4 also shows the XCO2 values increasing by about 10 ppm from September 2014 to September 2018. We note that no data are available at high middle-latitudes in autumn-winter when the Sun is too low for a successful XCO2 retrieval. Furthermore, a smaller amount of data is expected over areas frequently covered by clouds or with a large aerosol load.

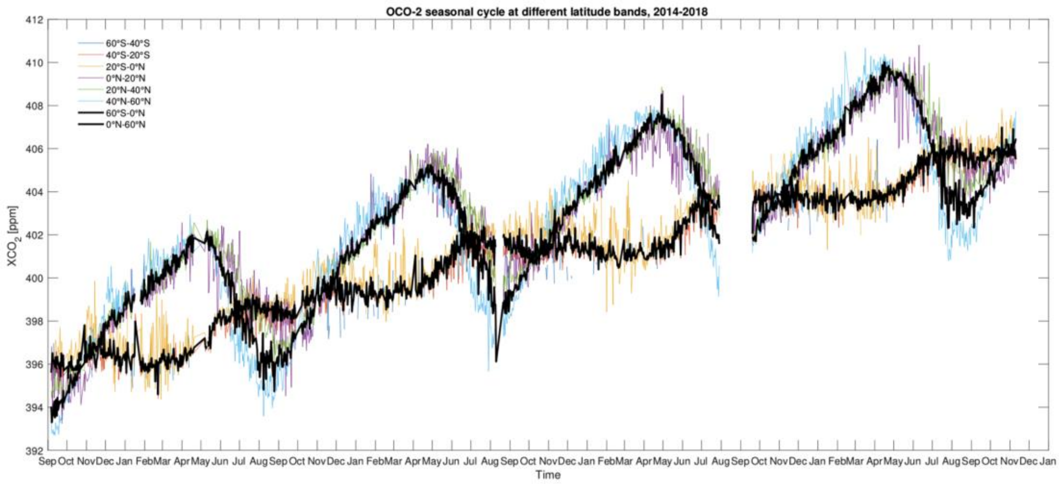

Figure 2 OCO-2 seasonal cycle at different latitude bands.

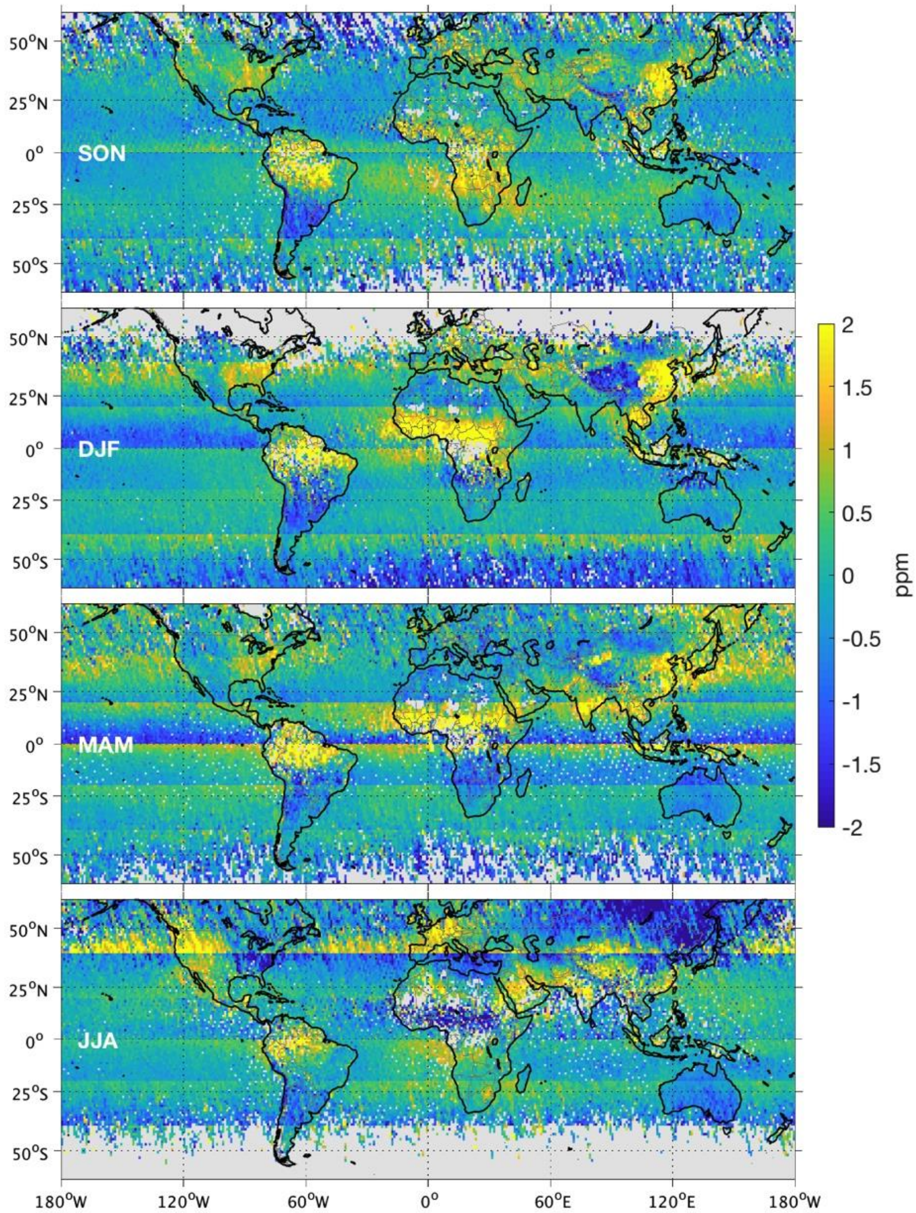

Figure 3 Seasonal OCO-2 XCO2 anomalies with respect to 20-degree latitude bands without interpolation. Latitudinal artifacts are observed.

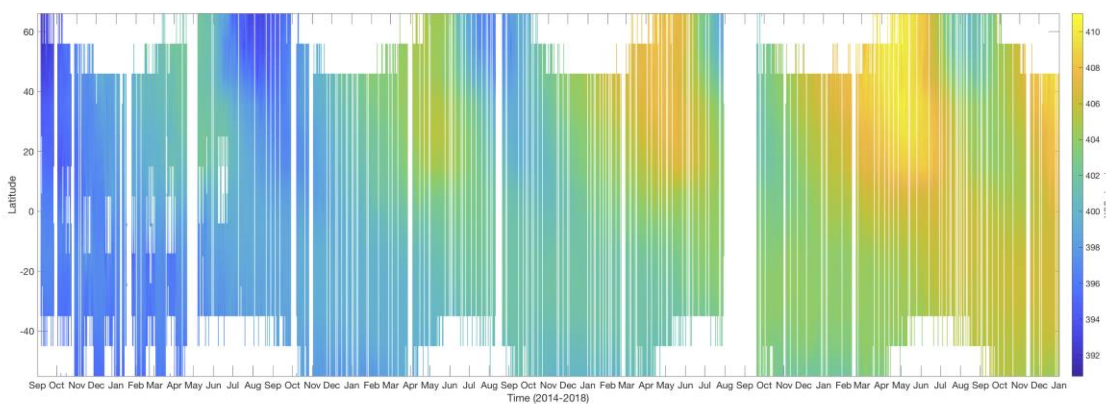

Figure 4 OCO-2 XCO2 daily background, 2014–2018. Daily medians are calculated for each 10-degree latitude bands and interpolated at 1-degree resolution.

2.1.3 Annual XCO2 anomalies

Figure 5 illustrates the mean OCO-2 XCO2 anomaly for 2015–2018 on 0.25°× 0.25° latitude-longitude grid. The largest anthropogenic anomalies correspond to the areas in China, North-East India, Middle East, central Europe, and eastern USA. In the Southern Hemisphere, the largest anthropogenic emission area, the Highveld region in South Africa, is clearly visible.

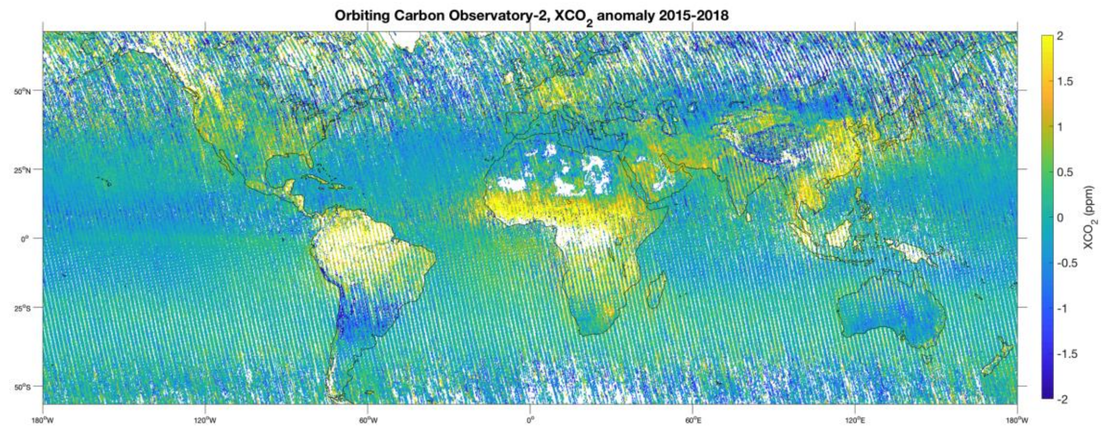

Figure 5 OCO-2 XCO2 anomaly, four-year average 2015-2018.

The largest positive XCO2 anomalies are observed in the tropical regions in northern and southern Africa, Indonesia, Indochina, and South America. These correspond to large-scale biomass burning and to positive biospheric fluxes (respiration). These anomalies are most intense during the 2015–2016 El Niño, but persist through the four-year period considered here.
The largest negative anomalies are observed in the northern middle-latitudes (40°N–60°N) over Asia and North America. These are clearly associated with the strong biospheric sink during the growing season. This area is mainly sampled by OCO-2 during summer months and not during winter due to persistent cloudiness and low signal levels at high solar zenith angles. This temporal sampling bias may introduce biases in the annual-average anomalies. We also observe a large area with negative anomalies in the Southern Cone in South America.

Figure 6 illustrates mean annual anomalies for the years 2015–2018. The large areas with positive and negative anomalies are quite consistent from year to year. Also, smaller areas with large anomalies seem to be consistently visible in all years (e.g., the Highveld region). Some differences in the XCO2 anomaly patterns between different years are, at least partly, related to the sampling of the instrument and the number of data points available. These are most visible for example at northern and southern mid-latitudes, where we can still identify individual “satellite tracks” from the map. In addition to northern latitudes, the number of data points is lower also in places with high cloud density and/or large aerosol load (Himalaya, Amazonia, central Africa and China). Thus, the anomalies calculated over these areas are less robust.

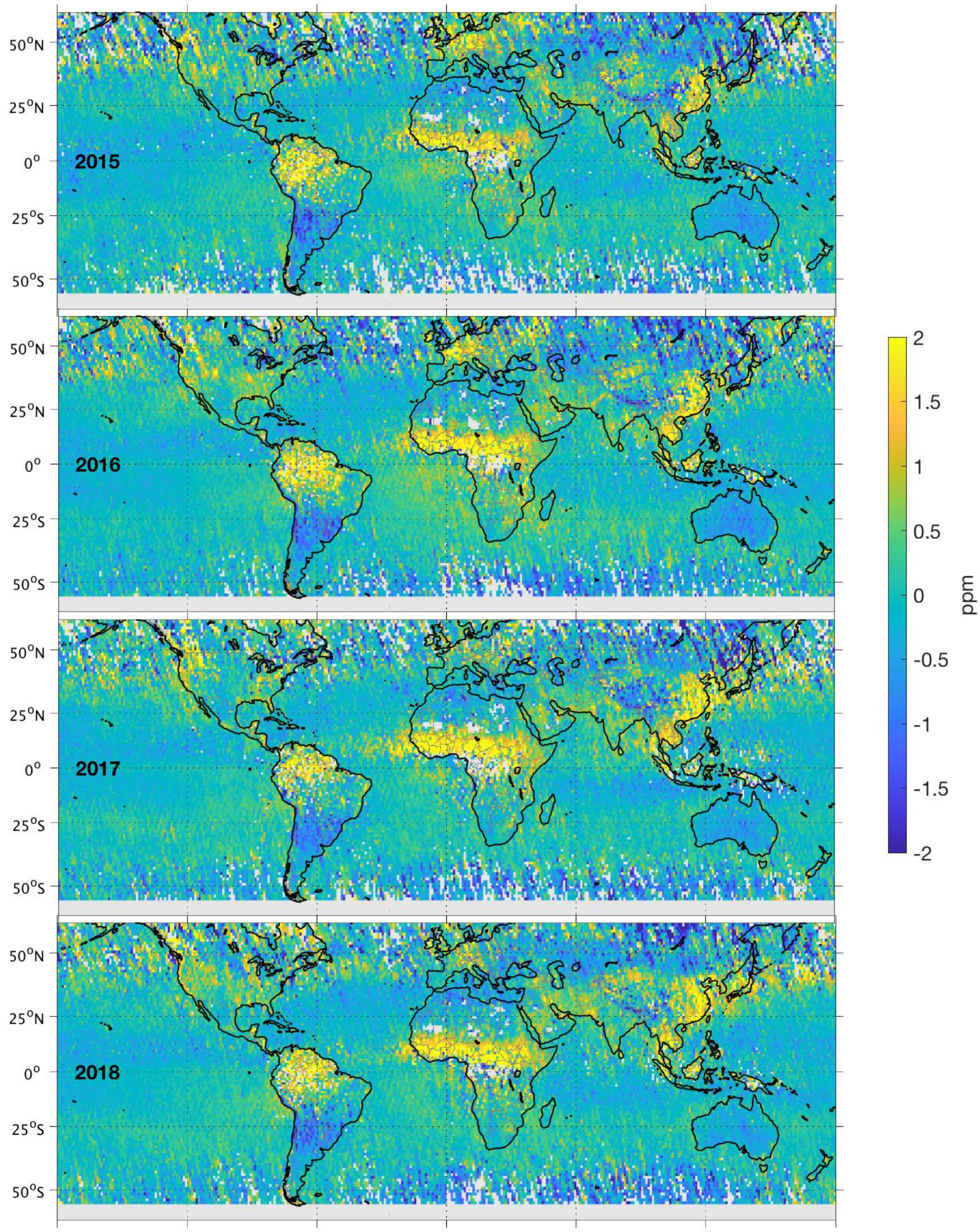

Figure 6 Annual mean OCO-2 XCO2 anomalies for the years 2015, 2016, 2017, and 2018, respectively.

Seasonal XCO2 anomalies

Figure 7 illustrates the mean seasonal XCO2 anomalies calculated from the period September 2014 to August 2018. The different seasons are defined as September-October-November (SON), December-January-February (DJF), March-April-May (MAM), and June-July-August (JJA). The large-scale patterns on SON, DJF, MAM look very similar to each other and to the annual mean, while in JJA the anomaly distribution looks quite different, with strong negative anomalies over the Northern Hemispheric mid-latitudes. We note that no OCO-2 observations are available during winter months (DJF) over the northern high- and mid-latitudes, due to persistent cloudiness and low signal levels.

In order to better understand this seasonal variability, we analyze the seasonal distribution of the SIF, also measured by OCO-2, as well as the fluxes from NOAA's CarbonTracker model (not shown in figures). Both SIF and CarbonTracker flux spatial distributions show how the negative anomalies observed during JJA are related to the biospheric sink (i.e., high SIF and negative fluxes). The XCO2 anomaly patterns in Africa show positive values in the northern biomass burning area during winter months (DJF) and relatively smaller anomalies during SON and MAM. During summer months, we find mainly negative XCO2 anomalies over the same area. These features correspond directly to those observed in the emission-based estimates, i.e., strong emissions from biomass burning during winter and uptake during summer. In the southern biomass burning area in Africa, we observe the largest XCO2 anomalies during SON and JJA, when the biomass burning emissions are the strongest (Figure 6, right column). The largest negative XCO2 anomalies are seen in DJF and MAM, when there are reduced emissions from biomass burning. From Figure 4, we find that the XCO2 anomalies over the Highveld area in South Africa are the largest during JJA and SON, when the CO2 uptake by photosynthesis is minimum.
In Indochina, negative XCO2 anomalies correspond to the largest SIF values observed during JJA, although from the biospheric flux maps, we would expect positive fluxes during JJA. During DJF and MAM, we see the signature of strong emission from fires in the anomalies and flux maps. We would expect however to see negative anomalies during SON due to the strong biospheric sink, but we find only slightly smaller positive anomalies. In the Indian peninsula we find positive XCO2 anomalies as expected from anthropogenic emissions when the biospheric uptake is low. Seasonal patterns are also evident in the largest anthropogenic emission areas, i.e., China, central Europe and eastern USA. For example, China and central Europe show positive anomalies during all seasons, while in eastern USA these are offset by a very strong biospheric sink in JJA. Also, the positive XCO2 anomalies in China and central Europe are lower during JJA and MAM, respectively.

Finally, we note signatures of outflow over the Atlantic Ocean with positive XCO2 anomalies from the biomass burning emissions in Africa. Furthermore, the springtime outflow along the dominant westerlies from China to North America is also visible, as also observed, e.g., for tropospheric ozone in several studies.

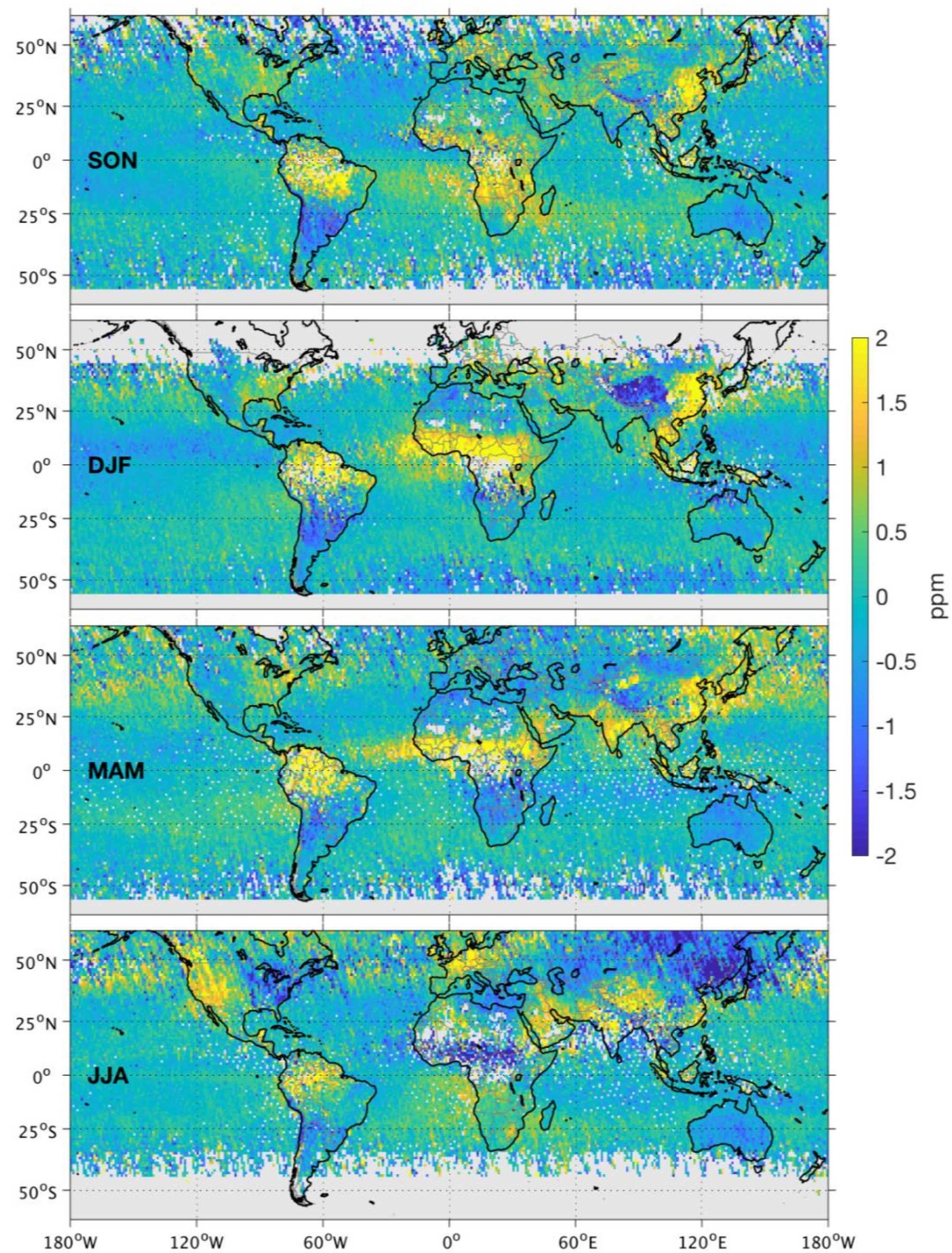

Figure 7 OCO-2 Seasonal XCO2 anomalies.

2.1.4 Comparison to inventory-based estimates

We analyze the XCO2 enhancements related to fossil fuel combustion and biospheric fluxes corresponding to the OCO-2 sounding footprints using the Lagrangian FLEXPART model. This allows us to account for the effect of the OCO-2 sampling as well as the transport by the wind. As input information for anthropogenic emissions, simulations use the high-resolution ODIAC (Open-Data Inventory for Anthropogenic Carbon dioxide; Oda et al., 2018) inventory, http://www.odiac.org/index.html. The FLEXPART simulations were provided by NIES and were available only with input on fossil fuel combustion and biospheric fluxes. Information on the biomass burning contribution was not included in the simulation.

Figure 8 illustrates the modeled XCO2 enhancements for the year 2015. We illustrate the contribution from the ODIAC fossil fuel fluxes alone (Figure 8, upper panel) and together with the biospheric contribution (Figure 8, lower panel). The anthropogenic component shows spatial patterns similar to those observed from the XCO2 anomalies, with high positive enhancements in eastern USA, Europe, India, Middle East and China. In the Southern Hemisphere, the Highveld region in South Africa shows the strongest anthropogenic signal, together with the area around Sidney in Australia. When adding the biospheric component, we also find negative values in the northern mid-latitudes and in the Southern Cone in South America, as observed from the anomalies. In Europe, the large anthropogenic XCO2 enhancements are drawn down by the biospheric sink (Figure 8, lower panel). The largest differences between the patterns in the FLEXPART simulations and the OCO-2 anomalies are in the tropical region, where the OCO-2 XCO2 anomalies show large positive values while the FLEXPART enhancements are close to zero. Part of the reason is that the FLEXPART simulations do not include the biomass burning contribution, but also the biospheric contribution is lower.

Figure 9 illustrates the results of the FLEXPART seasonal simulations. We find that the Highveld region is clearly visible during SON and JJA, while it is not detectable during DJF due to effect of the biospheric sink. The same feature is also visible in the seasonal anomalies in Figure 7. In addition, while OCO-2 shows negative XCO2 anomalies over central North America and South Central Asia during the fall (SON) and winter (DJF), the FLEXPART enhancements over both regions are positive. Four local "case studies" for both FLEXPART enhancements and OCO-2 anomalies are illustrated in Figure 10. The first one is the Iberian Peninsula, where OCO-2 XCO2 retrievals are available consistently throughout the year. Here, OCO-2 measurements indicate larger XCO2 anomalies over coastal cities than the model results. The second area is the Highveld industrial region in South Africa. In this case, the anthropogenic signatures seem more localized in the FLEXPART simulations than in the OCO-2 anomaly maps, although positive anomalies are clearly visible over the area as well. The third case study is over India, where we can see a clear positive signal in both OCO-2 and FLEXPART data, but the OCO-2 results indicate more discrete and localized anthropogenic emissions than the model results. The last case is Mexico City, where we also see strong anthropogenic signatures (i.e., positive enhancements and anomalies), related to the emissions from the city as well as the power plants in the area, with some differences in the locations of the positive enhancements. These differences may reflect uncertainties in the emission source intensities or locations or significant local wind data errors at low wind conditions while using wind data from global reanalysis.

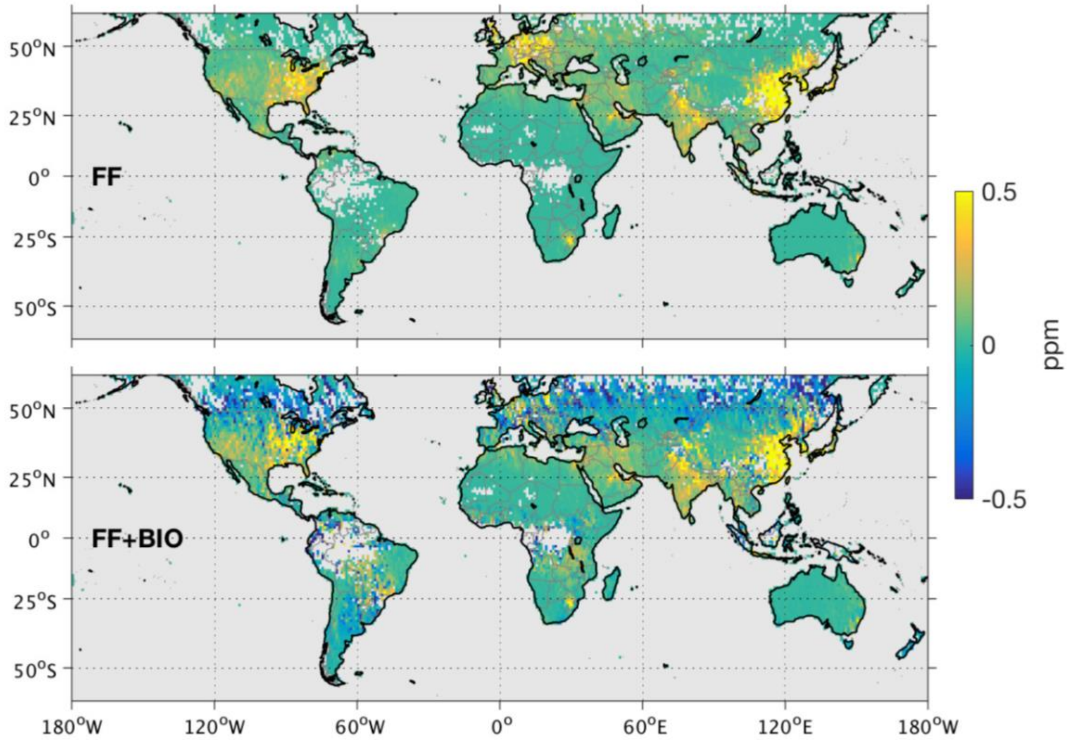

Figure 8 FLEXPART simulation results for the year 2015 with contribution from fossil fuel combustion (FF) only and also with biospheric component (FF + BIO).

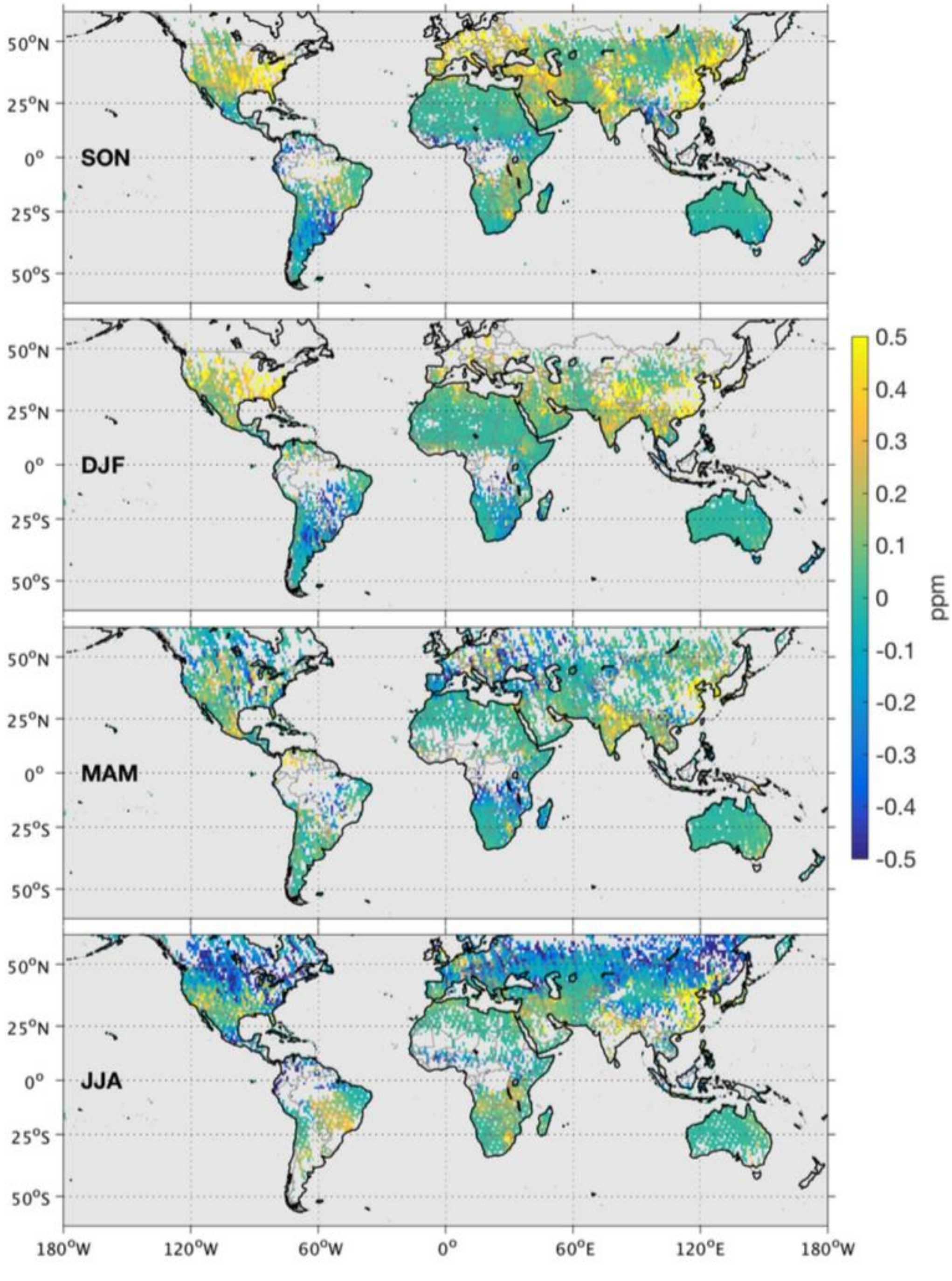

Figure 9 FLEXPART seasonal XCO2 enhancement simulations from September 2014 to August 2015, including fossil fuel and biospheric contribution (FF + BIO).

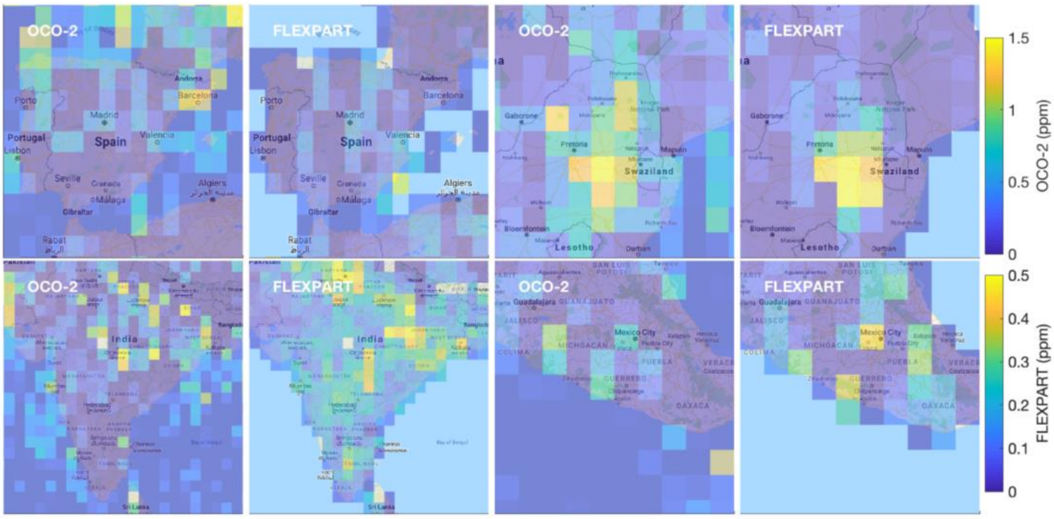

Figure 10 Case studies for the year 2015: Iberian Peninsula, Highveld industrial region in South Africa, India, and Central America. OCO-2 XCO2 anomalies and FLEXPART XCO2 enhancements are overlapped to the Google map background.

2.1.5 Comparison between different OCO-2 data versions

The figures below show the annual mean hemispheric XCO2 anomaly for the year 2016 for OCO-2 V7r, V8r, and V9r datasets, respectively. The algorithm changes are summarized in Table 1. The largest changes happened between V7 and V8, and were related to calibration as well as to the inclusion of an optically thin, upper-tropospheric/lower stratospheric aerosol type. The change between V8 and V9 was less drastic, and was related to, e.g. point errors, filtering and surface pressure. We observe differences in the absolute values, but the overall patterns do not change.

Table 1 Summary of the OCO-2 algorithm changes compared to previous version

Algorithm version	Changes compared to previous version
V8	• L1B calibration • inclusion of an optically thin, upper-tropospheric/lower stratospheric aerosol type
V9	• corrected point errors • more relaxed filtering • improved surface pressure
V10	• L1B calibration • *a priori* information for aerosols and CO_2 • treatment of the surface albedo

Figure 14, shows the difference between V7 and V9. The largest differences are visible over Himalaya and tropics. We expect most of the differences related to algorithmic changes, but we note that there are different numbers of data points in each dataset. For example, in V9r we observe more data over Amazonia, due to more relaxed quality filtering. The analysis of the preliminary OCO-2 XCO2 V10 retrievals is presented in Figure 15 for the year 2015. The comparison of the anomalies reveals for example that in general, the amplitude and spatial extent of the positive anomaly over central and northern Africa in the V9 product is reduced in V10, while the amplitude and spatial extent of the positive anomalies over southern Africa and the Amazon are slightly increased in V10. The negative anomalies in the V9 product over Australia vanish and the spatial extent of the negative anomaly over the cone of South America is reduced. The negative anomaly over the Himalaya plateau and over the boreal region is enhanced in this version of V10. The overall impact of these changes appears to be a small reduction in the land-ocean contrast.

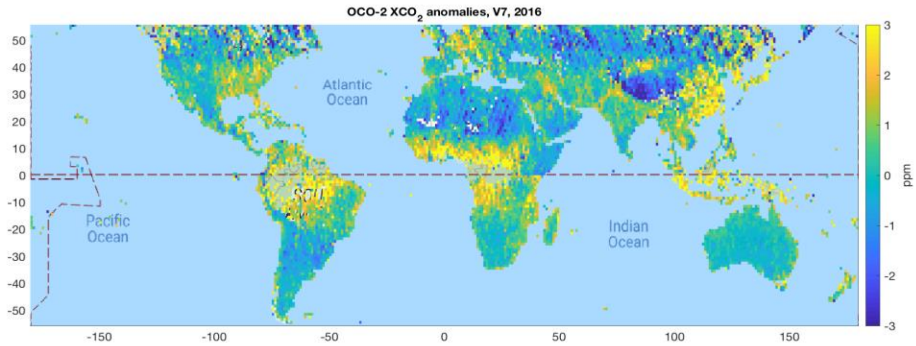

Figure 11 OCO-2 mean hemispheric XCO2 anomaly for the year 2016, V7r.

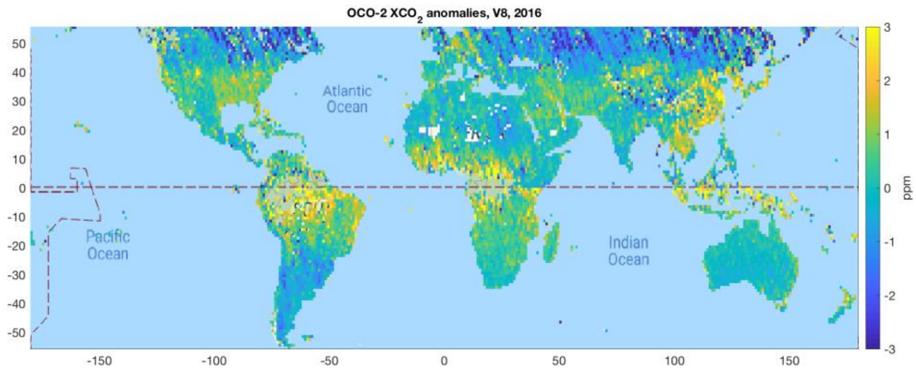

Figure 12 OCO-2 mean XCO2 anomaly for the year 2016, V8r.

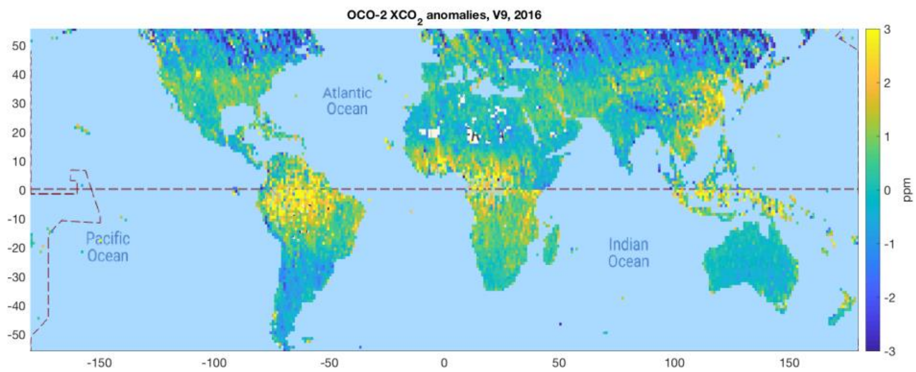

Figure 13 OCO-2 mean XCO2 anomaly for the year 2016, V9r.

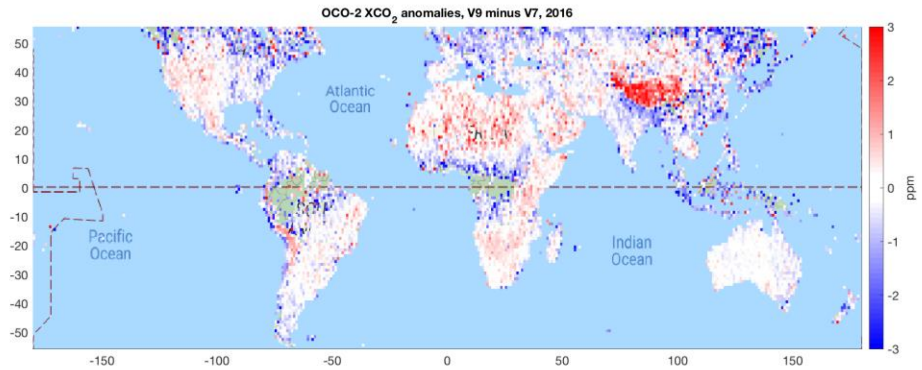

Figure 14 The absolute difference between V9r and V7r XCO2 anomalies.

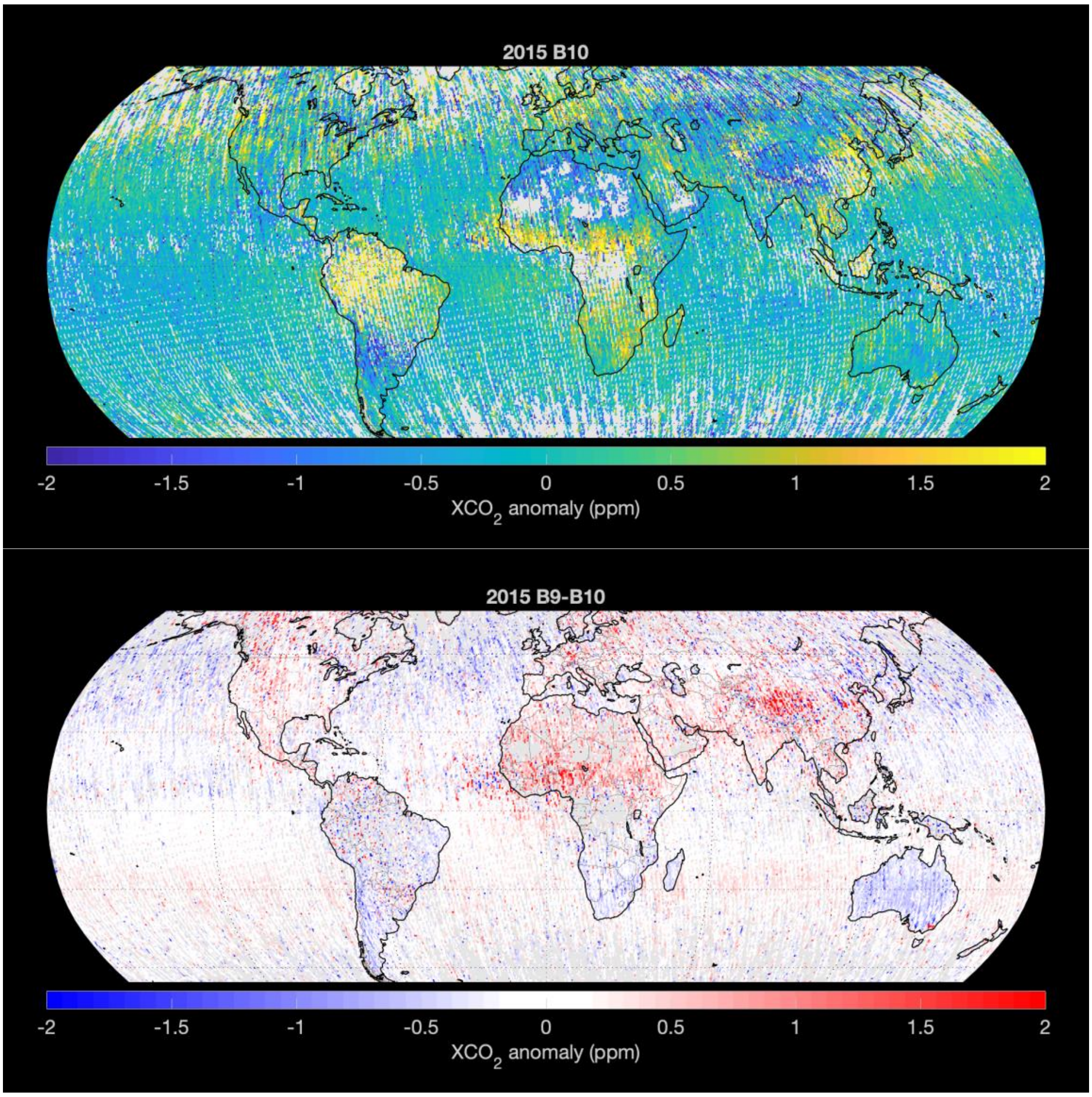

Figure 15 Upper panel: OCO-2 mean XCO2 anomaly for the year 2015, Version 10. Lower panel: Difference between XCO2 anomalies V9 minus V10. Red (Blue) colors correspond to V9 larger (smaller) than V10.

2.1.6 S5P and OCO-2 Collocation

We analyze one full year (from February 2018 to January 2019) of S5P/TROPOMI data together with OCO-2 observations. We used S5P NO2 and CO operational products available since February 2018.

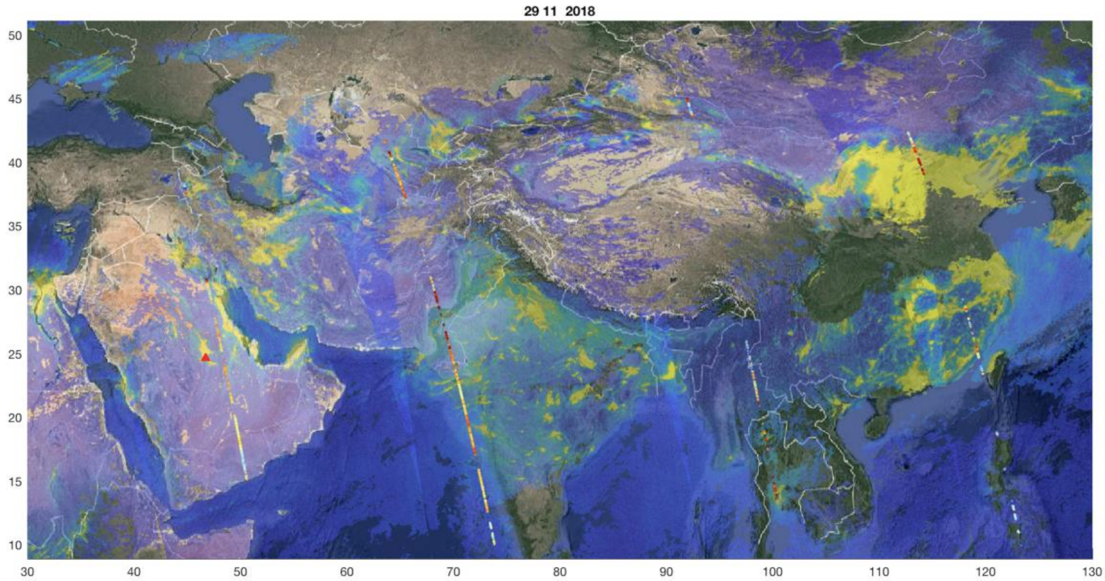

Figure 16 Example of OCO-2 XCO2 anomalies over S5P tropospheric NO2 columns during one day (29 November 2019).

Figure 16 illustrates one day of S5P tropospheric NO2 map overlaid with OCO-2 XCO2 anomalies. TROPOMI has a swath of about 2600 km and OCO-2 less than 10 km. TROPOMI has a spatial resolution of 7×3.5km2 at nadir for bands 2–6 (UVN), 7×7km2 at nadir for bands 7 and 8 (SWIR), and 21 × 28 km2 at nadir for band 1 (deep UV). Before collocating the data we apply data screening for each dataset. For OCO-2, we use the lite files that include bias correction and most of the data screening. We use data points from all three science viewing modes, where the quality flags are set to zero, indicating highest quality data. For TROPOMI NO2 we ignore the fields with data quality value less than 0.75. In addition, we ignore the fields with SZA higher than 85° and cloud fraction higher than 0.3. For the TROPOMI CO products, we ignore the fields with data quality value less than 0.5 and SZA higher than 85°.

As the OCO-2 ground track is narrower, and because in this study CO2 is of our primary interest, we search TROPOMI co-location for each OCO-2 measurement point.

For collocating we have three criteria:

1. The temporal distance is less than one hour.
2. Distance in longitude is less than 0.07 degree.
3. Distance in latitude is less than 0.07 degree.

If several TROPOMI data points are found, we select the closest one. We perform the collocation separately for TROPOMI NO2 and CO dataset. While the collocations are derived daily, we analyze the average values over a long time period (e.g., 3 months, 1 year). For the local plume analysis (Sect. 2.2) only the collocation between NO2 and XCO2 anomalies are taken into account. All TROPOMI pixels across the swath have been included in the analysis. The difference in pixel dimension across-track is quite small (from 3.7 km at nadir to about 10 km at the edge of the swath) for TROPOMI compared to previous instrument (e.g., OMI). This affects more the local scale analysis than the global anomalies.

Figure 17 illustrates the collocated datasets of XCO2 anomalies, NO2 and CO from February 2018 to January 2018 on 0.25°× 0.25°, latitude-longitude grid. We require that all three data points are available. The largest effect comes from the OCO-2 sampling. Over oceans the CO limits the number of collocations, as there would be more NO2-to-CO2 collocations, but over land the difference is negligible (not shown in figures). We observe similar patterns in all datasets, but the anthropogenic features are most visible in CO2 and NO2 dataset. For example in Highveld area in South Africa we can see anthropogenic signatures in both NO2 and CO2, but not in CO. Same is true also for example for the costal cities of Australia or for Middle East. Figure 18 illustrates the seasonal average from December 2018 to January 2019. From this two-month average we can observe biomass burning in northern Africa and Indochina. In India, we see high CO patterns but less clear for CO2.

We also analysed the CO2/NO2 ratio on global scale (see Figure 19) for relatively large values of NO2. We find higher ratios over biomass burning areas while lower ratios over industrial areas. In particular, the Highveld region in South Africa, India and North-East China show low values of the ratio, corresponding to high levels of pollution. As in the results from the cluster analysis, the biomass burning areas over Angola, Congo and Zambia low ratio while the larger forest fire region below the Sahara shows high values of the ratio (as expected for biomass burning areas where the CO2 emission are proportionally larger than NO2, compared to areas dominated by anthropogenic emissions).

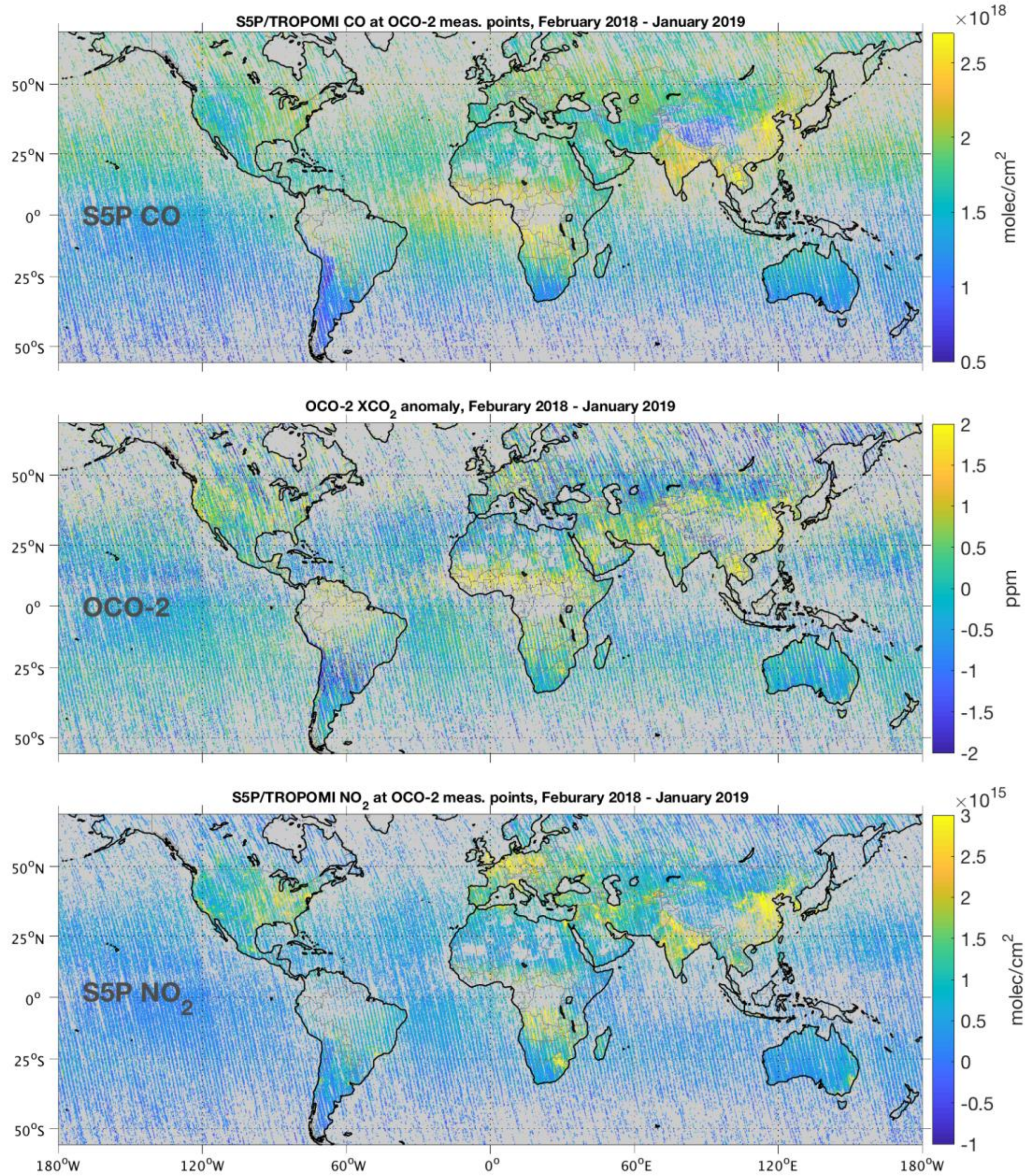

Figure 17 Collocated OCO-2 and S5P observations for one year (from February 2018 to January 2019).

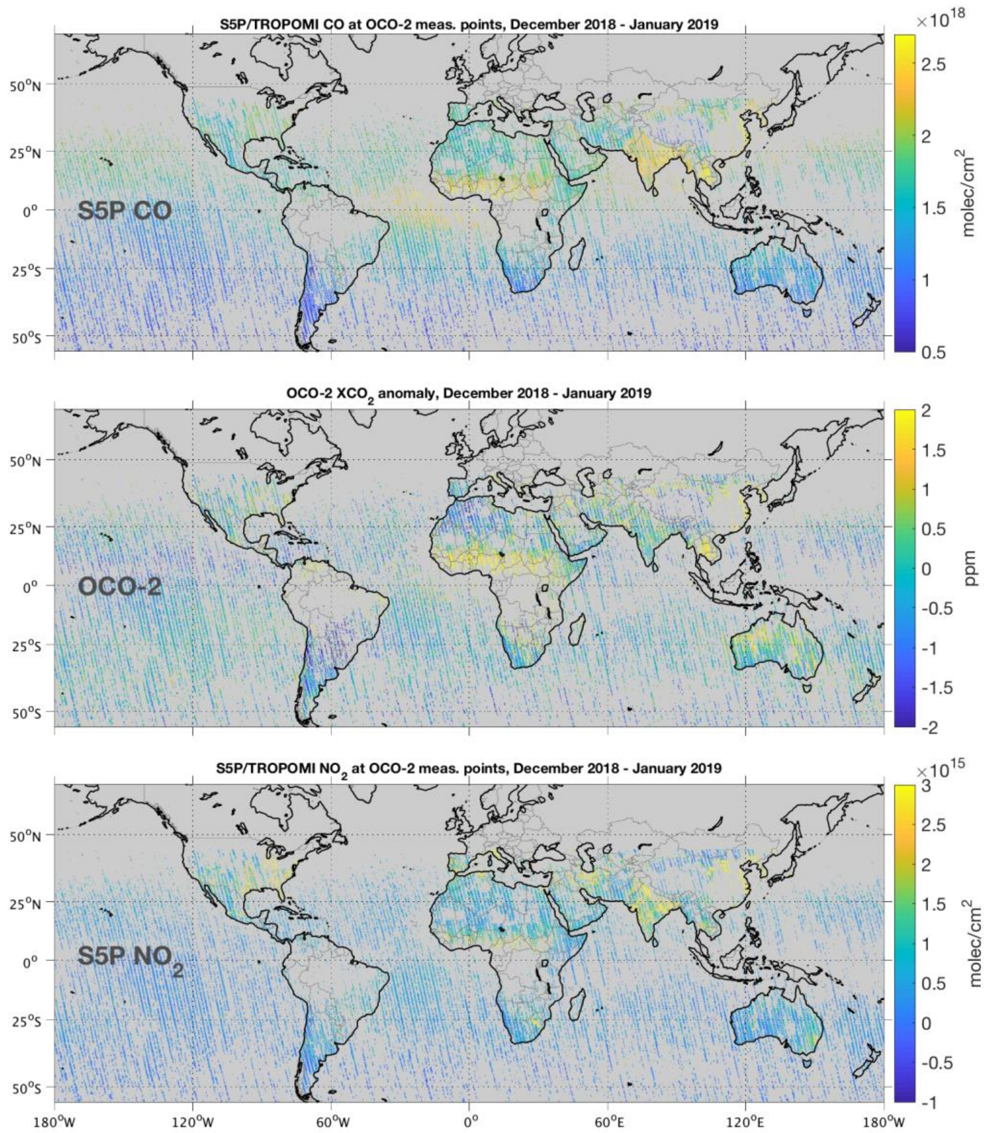

Figure 18 Collocated OCO-2 and S5P observations from December 2018 to January 2019.

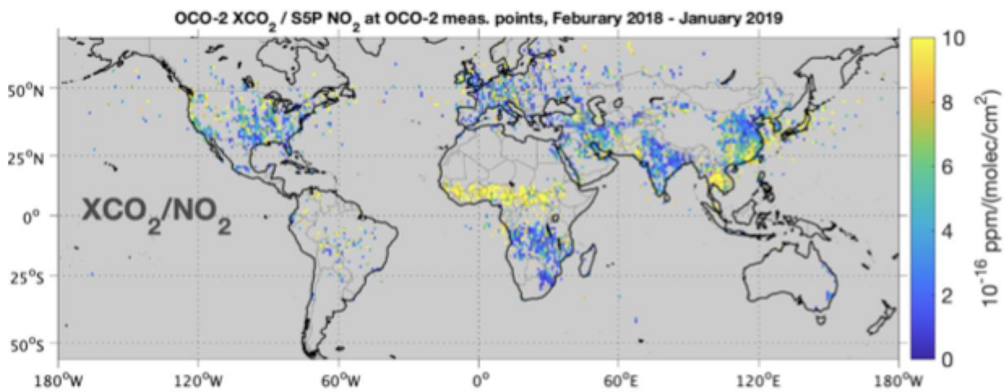

Figure 19 Ratio between OCO-2 XCO2 anomalies and TROPOMI NO2 tropospheric columns

2.1.7 Cluster analysis

In order to separate different emission areas, we use clustering methods based on unsupervised machine learning: K means clustering and Expectation-Maximization (EM) clustering. The first method is based on mean Euclidian distance between the data points, whereas the latter is based on mixture of Gaussian distributions. Both methods operate in two steps, assignment (expectation) and update (maximization), and run until convergence is achieved. K means clustering is first applied, and the results are then used as an input for the EM clustering.

In Hakkarainen et al. (2016) we applied cluster analysis (in order to combine the information) for V7r XCO_2 anomalies and OMI NO_2 mean fields. At that time it was not possible to collocate OCO-2 and OMI data as OCO-2 flies inside the so-called OMI row anomaly. Here we apply cluster analysis to collocated OCO-2 XCO_2 anomalies, TROPOMI NO_2 and CO, as presented in the previous section. We screen the data for land pixels only. The data are gridded on $1° \times 1°$ latitude-longitude grid in order to reduce the noise and to more easily interpret the clustering results.
Figure 20 illustrates the pair-wise scatter plots. The cluster analysis is done together for all three datasets; we start from random initial values and use seven different clusters. The clusters are colored based on their mean NO_2 value for visual purposes. For example, in the cluster #7, we observe high NO_2, CO and CO_2 anomalies. This cluster is related to strongest anthropogenic emission areas. In cluster #5, both CO and CO_2 anomalies are high as in cluster #7, but NO_2 values are only slightly enhanced, which corresponds to biomass burning areas. The results are presented also as maps in Figure 21. We observe quite natural progression between the clusters, even though there are no spatial constraints in the clustering (or any other geographical information). The cluster #7 is related to the anthropogenic emission areas, and the members of this cluster are located where the NO_2 levels are typically highest. The cluster #6 is related to the second highest NO_2 regions, but also part of Africa is included in this cluster. As these values are not related to anthropogenic emissions, but to biomass burning, we tested if these values can be separated. In Figure 22, we mark these points with black stars on the map as well as in pair-wise scatter plots (Figure 23). We note that the discrimination based purely on data values would be nearly impossible over this area. The cluster #5 highlights the biomass burning areas in Africa and Indochina. From Figure 17 we observe quite different features in the northern and southern biomass burning areas in Africa. In the northern part, the XCO_2 anomalies are much stronger, but less NO_2 is observed. In the southern part, the contrary is true. Cluster #4 is mostly located in Europe and North America, and corresponds to “urban background” conditions. The remaining clusters are not related to anthropogenic emission sources.

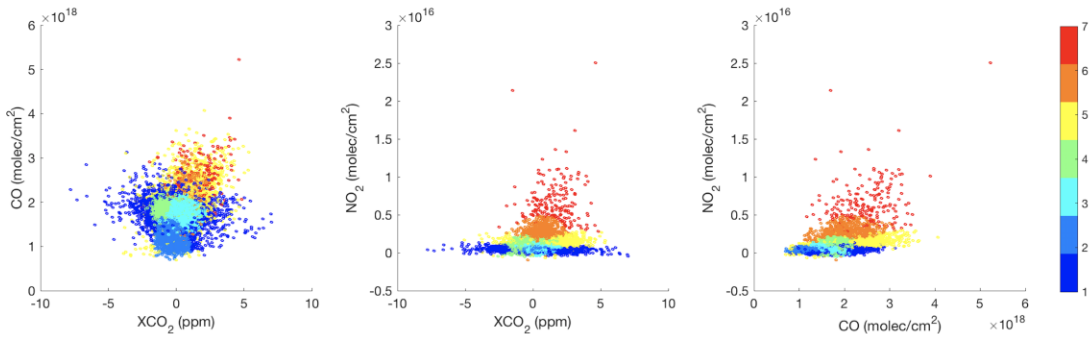

Figure 20 Scatterplots between collocated OCO-2 XCO2 anomalies and TROPOMI NO2 and CO columns. Color indicates the cluster number.

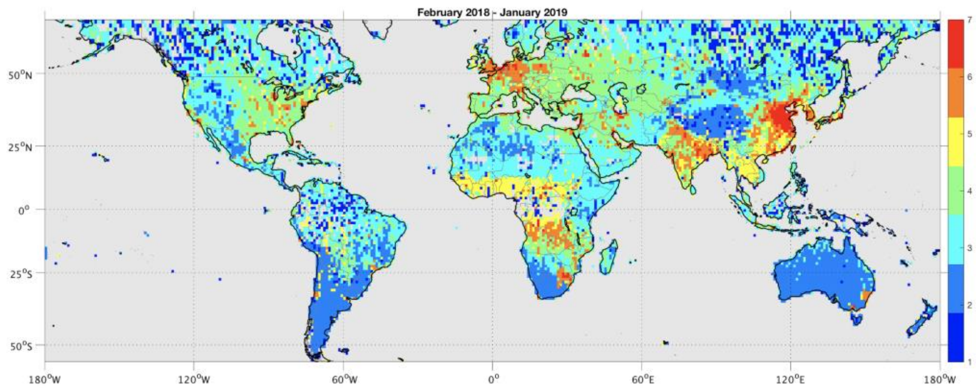

Figure 21 Map of the different clusters. Note that no geographical information was used in the clustering.

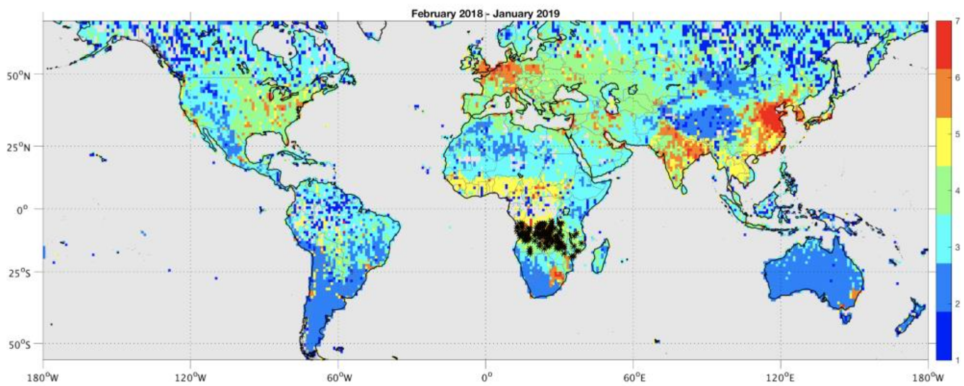

Figure 22 Same as Figure 21, but the area in Africa is highlighted with black stars.

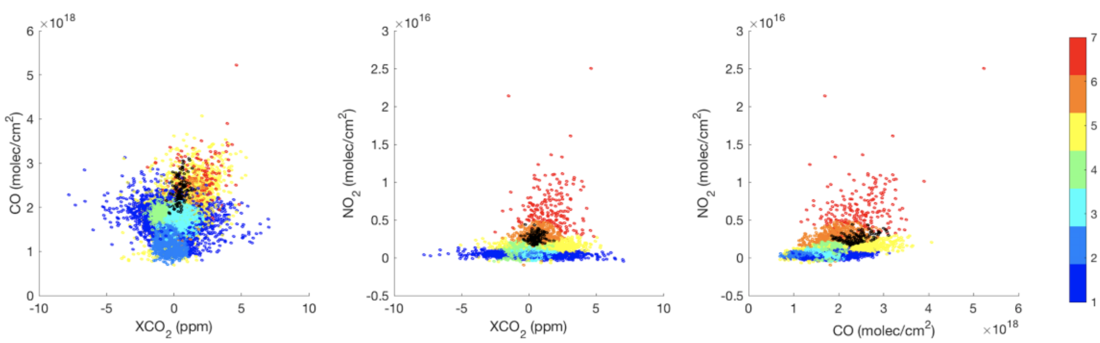

Figure 23 Same as Figure 20, but the area in Africa is highlighted with black stars.

2.2 Local plumes analysis

2.2.1 Plume detection method

Figure 16 in Section 2.1.6 illustrates one day (29 November 2019) of S5P tropospheric NO2 columns overlaid by OCO-2 XCO2 anomalies. We note how TROPOMI has a much larger swath (about 2600 km) than OCO-2 (less than 10 km). We can visually note the correlation between XCO2 anomalies and tropospheric NO2, with large NO2 values often corresponding to high XCO2 anomalies. The main idea for the local plume detection is to use NO2 as proxy for CO2, as they are often co-emitted, in order to detect anthropogenic plumes. Due to the short lifetime of NO2 and to the much wider swath of TROPOMI, detecting plumes with TROPOMI/S5P is much easier than with OCO-2. Using NO2 fields will enable to locate the anthropogenic CO2 plumes generated from a certain source that would be difficult to identify otherwise. Before the plume identification, the data have been screened and collocated as described in Section 2.1.6. If several TROPOMI data points are found, the closest one was selected. We used two methods for detecting plumes:

Method1: If we have a source of interest, e.g., an individual city or power plant, we can select an area around the source, for example a box centered in the source of interest ±2 degrees in longitude and ±2 degrees in latitude. We can quickly select all the S5P and OCO-2 available during a day, and automate a script that prints a map only if data from both datasets are available. Furthermore we can focus on collocation with NO2 values higher than certain threshold (e.g., 10^{16} molec./cm^2), in order to focus on areas with anthropogenic emissions. This procedure produces a set of maps that can be explored for further analysis. Figure 24 (left panel) shows an example of such maps showing a NO2 plume (yellow pixels on the background) originating from Matimba power station in South Africa overlaid with local XCO2 anomalies calculated from OCO-2 observations. We note how the XCO2 anomalies (red pixels in the OCO-2 swath) sharply increase inside the NO2 plume (area with yellow pixels).

Method 2: The second method is similar to the first one, except that we do not have a direct source available, so we go through maps covering larger areas and try to locate interesting sources that are not known beforehand (like largest power plants and cities). Also we use ECMWF ERA5 10 m wind speed and direction in order to better identify the source of pollution and the direction of the plume.

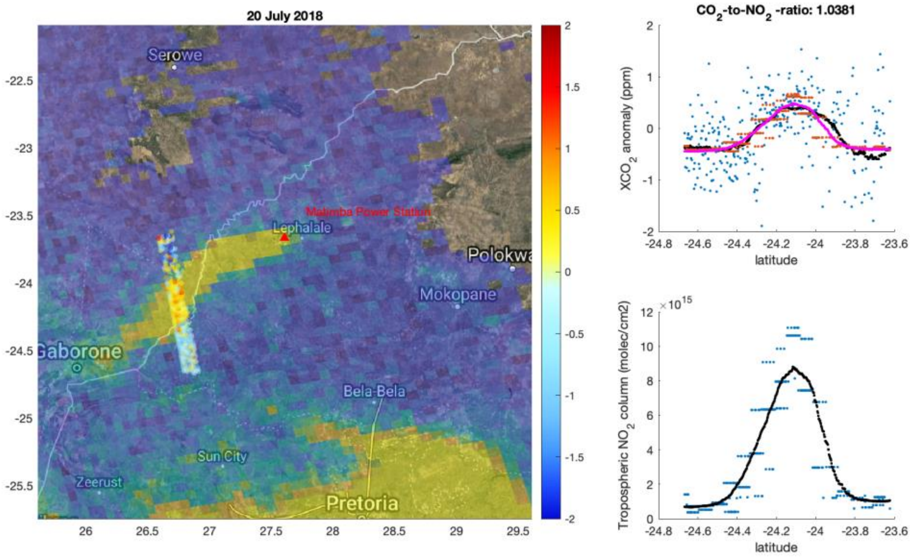

Figure 24 Example of plume detection using S5P NO2 and OCO-2 XCO2 anomalies (20 July 2018). The plume is originating from Matimba power station. The panels on right site of the figure correspond to the tropospheric NO2 and XCO2 anomaly collocations as a function of latitude. The running means are indicated in black lines. We also apply linear regression to transform tropospheric NO2 to XCO2 (magenta for running mean and orange for individual points).

The figures below illustrate some additional examples of collocations between S5P and OCO-2 observations. CO2-to-NO2 ratio and the different techniques for emission estimation will be discussed in the following sections. The maps show the S5P/TROPOMI tropospheric NO2 observations overlaid with OCO-2 XCO2 local anomalies (narrow track). The collocated values are presented in the subplots on the right side of the figures as a function of latitude. The running means are indicated in black lines. We also apply linear regression to transform tropospheric NO2 to XCO2 (magenta for running mean and orange for individual points).

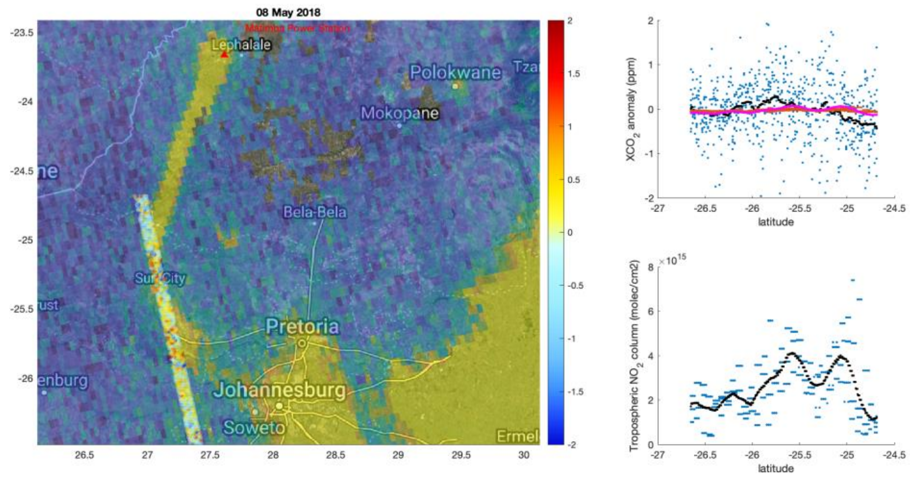

Figure 25 As Figure 24 but for 8 May 2018. The plume is originating from Matimba power station but the collocation is observed hundreds of kilometers from the emission source.

Figure 25 illustrates another collocation in South Africa, with the plume originating from Matimba power station. The collocation is hundreds of kilometers from the emission source. Figure 26 illustrates another case over the same area, where we find good agreement between NO2 and CO2 patterns also over the industrial area East of the city of Pretoria (south of the Matimba power plant).

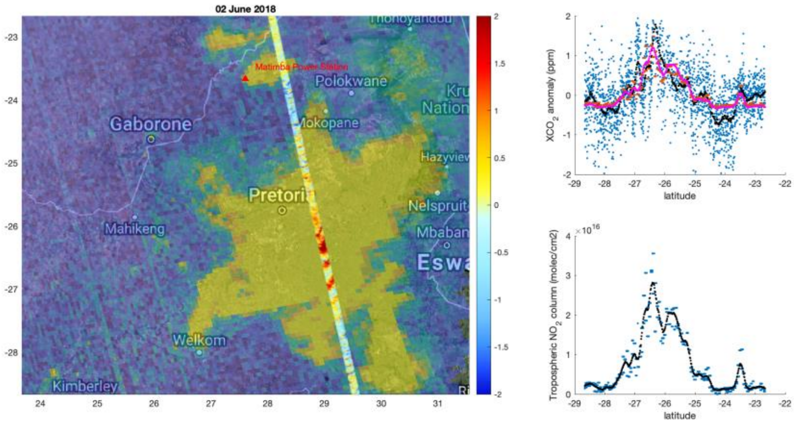

Figure 26 As Figure 24 but for 2 June 2018. Good correlation between NO2 and CO2 enhancements both in the plume originating from Matimba power station as well as in the industrial area East of the city of Pretoria.

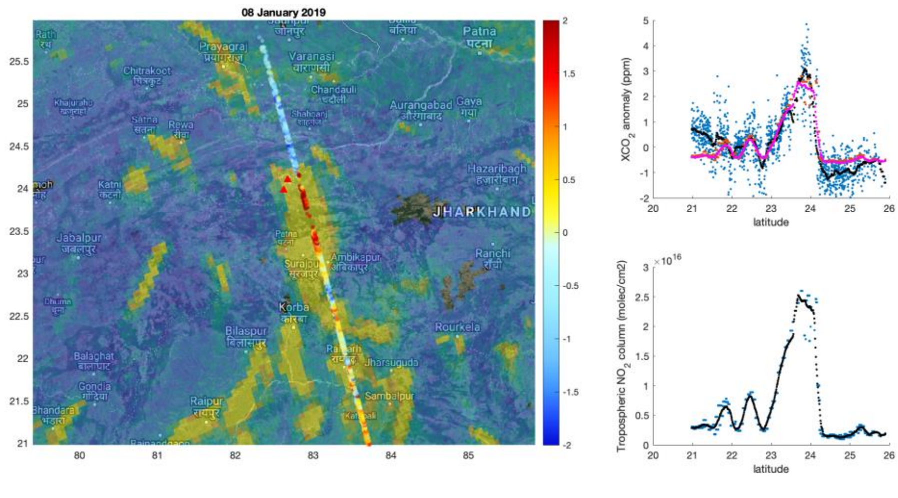

Figure 27 As Figure 24 but over India power plants and for 6 January 2019. The OCO-2 track goes through the NO2 plume and the XCO2 show a decay along the track.

Figure 27 illustrates a collocation over two power plants in India (Sasan and Vindhyachal). The OCO-2 track goes right though a NO2 plume originating from two power stations and the XCO2 decay along the plume can be clearly observed. The XCO2 anomaly values decrease from about 4 ppm close to the source to about zero moving south. The NO2 and XCO2 running means show similar patterns as well (Figure 27, top right panel). The NO2 fields also show plumes generated from several other sources.

2.2.2 Analysis of CO_2-to-NO_2 ratios

In the previous section we showed several collocations between S5P NO2 and OCO-2 CO2 observations, corresponding for example to emission plumes originating from individual power stations. From such collocations, CO2-to-NO2 ratio can be calculated and analyzed in order to identify different types of the emission source. The same ratio could also be potentially used in emission estimation, as estimating NO2 emissions is generally easier than estimating CO2 emission using observations from current space-based instruments.

Hakkarainen et al., (2019) analysed the XCO2 anomalies in South Africa for six days in July 2018 together with S5P NO2 tropospheric columns. Figure 28 illustrates the normalized histograms of OCO-2 XCO2 anomalies labeled as "anthropogenic" and "surrounding," discriminated according the tropospheric NO2 values (larger or smaller than 5×10^{15} molec./cm^2, respectively). In all cases, we note that the anthropogenic histograms peak at higher positive XCO2 anomalies than the histogram for the surrounding. Figure 29 illustrates the correlation between the median NO2 and XCO2 anomaly values inside and outside the NO2 plume as well as the difference between the values inside and outside the plume for each of the six days. We note that the points outside the NO2 plumes (red dots) fall into the bottom-left part of the scatter plot, corresponding to negative XCO2 anomalies and relatively low NO2 levels. Meanwhile, the points falling inside the plume with enhanced NO2 levels (blue dots) show a positive linear correlation between the median NO2 tropospheric columns and XCO2 anomalies. A similar correlation is observed for the differences between the values inside and outside the plume (yellow dots). In both cases, the slope of the linear fit, or the CO2-to-NO2 ratio, is about 1.5×10^{-16} ppm/(molec./cm^2). Among these six days, we observed two direct cross-sections of anthropogenic plumes originating from Matimba power station. Figure 30 illustrates these cross sections (11 and 20 July 2018). Black dots show the OCO-2 XCO2 values as a function of latitude during both days. The figure also includes the XCO2 values obtained by empirically converting TROPOMI NO2 tropospheric columns (collocated to the OCO-2 measurements) into XCO2 using the results of the linear regression between the two data sets (red dots). The CO2-to-NO2 ratio in both cases was about 10^{-16} ppm/(molec./cm^2).

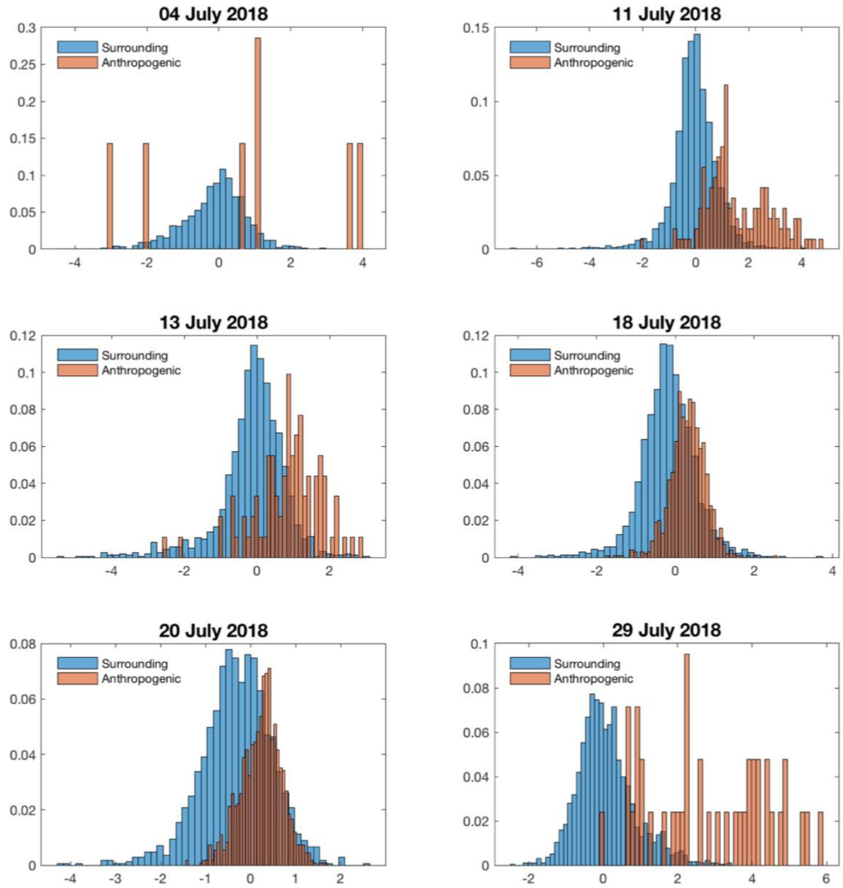

Figure 28 Histograms of XCO2 anomalies inside and outside the NO2 plumes. The anthropogenic and surrounding categories are discriminated according to the collocated tropospheric NO2 column values.

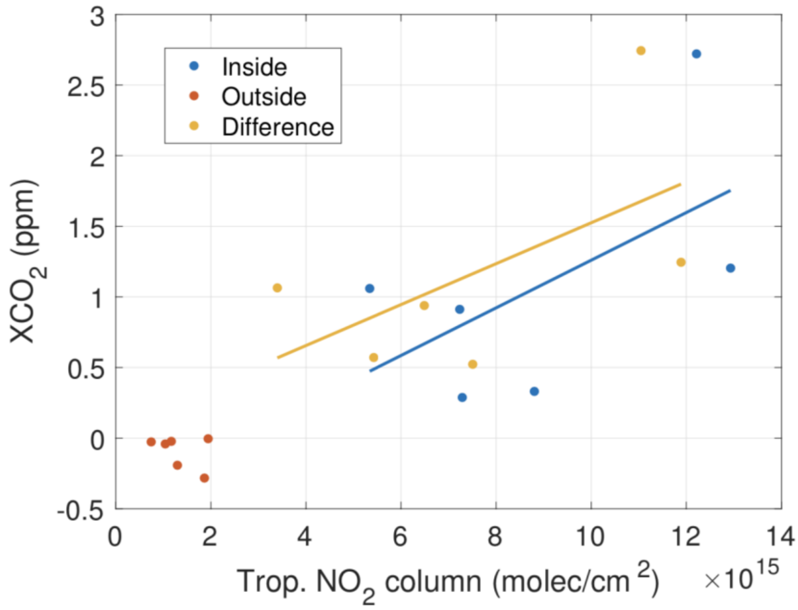

Figure 29 Scatterplot between the median XCO2 anomalies and tropospheric NO2 columns inside (blue dots) and outside (red dots) the NO2 plumes. The difference between the values inside and outside the plume is also shown (yellow dots). The corresponding linear fits are also shown (blue and yellow line).

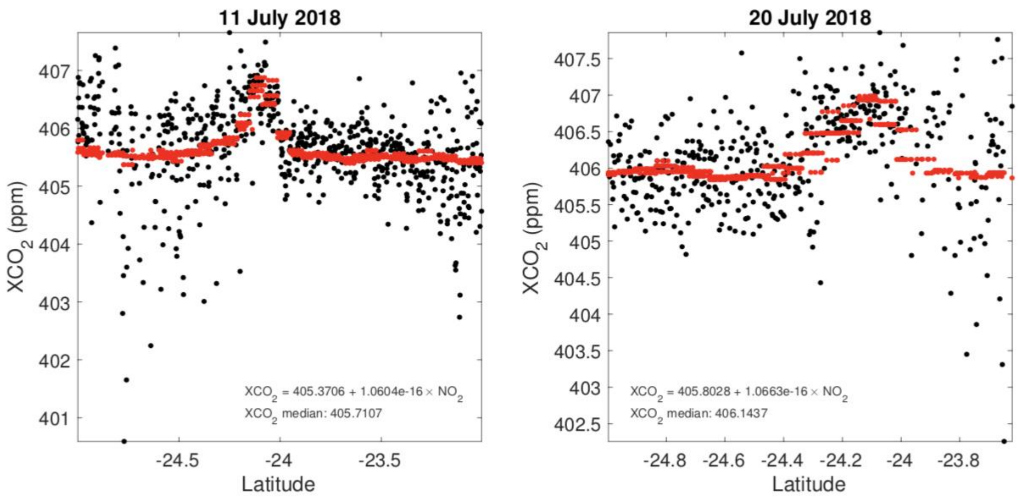

Figure 30 OCO-2 XCO2 values (black dots) as a function of latitude on 11 July 2018 and 20 July 2018. The enhancement corresponds to plumes originating from Matimba coal-fired power plants. The red dots indicate the XCO2 values obtained by converting TROPOMI NO2 tropospheric columns (collocated to the OCO-2 measurements) into XCO2 using the results of the linear regression between the two data sets.

In the figures below we present a few additional examples of the calculation of CO2-to-NO2 ratio at several locations. The CO2-to-NO2 ratio is determined as a slope of a linear fit. The CO2-to-NO2 value is affected by several factors other than the actual emission ratio of the source. For example the NO2 lifetime, distance from the source, wind and seasonality can have their effect. We note that the fit slope can be approximated by the ratio between the XCO2 anomaly and tropospheric NO2 peak values. The CO2-to-NO2 ratio is given at the top right of the figures in units of 10^{-16} ppm/(molec/cm^2).

Figure 31 show six overpasses near Sasan and Vindhyachal power stations in India. On 22 February 2018, 24 March 2018 and 11 March 2019, we obtain a CO2-to-NO2 ratio of about 1. On 24 March 2018 the overpass occurs very close to sources. On this day the NO2 peak is about 4×10^{16} molec/cm^2 and the XCO2 peak is 4 ppm. On 2 October 2018, the XCO2 anomaly enhancement is detected near the source, but the fit is much more challenging due to missing data and we obtain a ratio of about 1.5. On 3 November we observe a ratio of about 1.7 but again with a lot of missing data along the OCO-2 track. On 8 January 2019, we find good correlation between XCO2 anomalies and S5P tropospheric NO2 as the OCO-2 track goes parallel to the plume. On this day, we obtain a constant ratio of about 1.5.

The Iberian Peninsula offers quite many interesting emission hot spots. One of them is the city of Madrid, Spain. Four overpasses are shown in Figure 32 with CO2-to-NO2 ratio ranging between 0.7 and 2. In all four cases the CO2 patterns look quite similar, but the NO2 values vary depending on the season, wind conditions (and lifetime) during these days.

Figure 33 shows a few overpasses over the city of Moskov (Russia). On 31 July we observe a cross-section of the plume quite distant of the city and ratio of about 2. On 25 August we observe the emission from Moscow and also a second plume from Lipetsk steel plant. Over Moscow we obtain a ratio of about 0.6 and over Lipetsk a ratio of about 2.9. In the latter case we observe very high XCO2 anomalies of about 5 ppms, but this day was the only good collocation between S5P and OCO-2 over Lipetsk.

Finally, Figure 34 shows several overpasses over the city of Los Angeles, USA. There we have several overpasses with similar contrast between inside and outside the plumes (NO2 enhancements), but the fit between NO2 and CO2 is not always accurate. The ratios vary substantially from day-to-day. If we extend the area of study, we can observe many other anthropogenic signatures above Los Angeles. Both NO2 and CO2 observations show enhancements in the same places, but the magnitude of the NO2 enhancements vary more where as the maximum CO2 levels are rather constant (thus, producing different CO2-to-NO2 ratios).

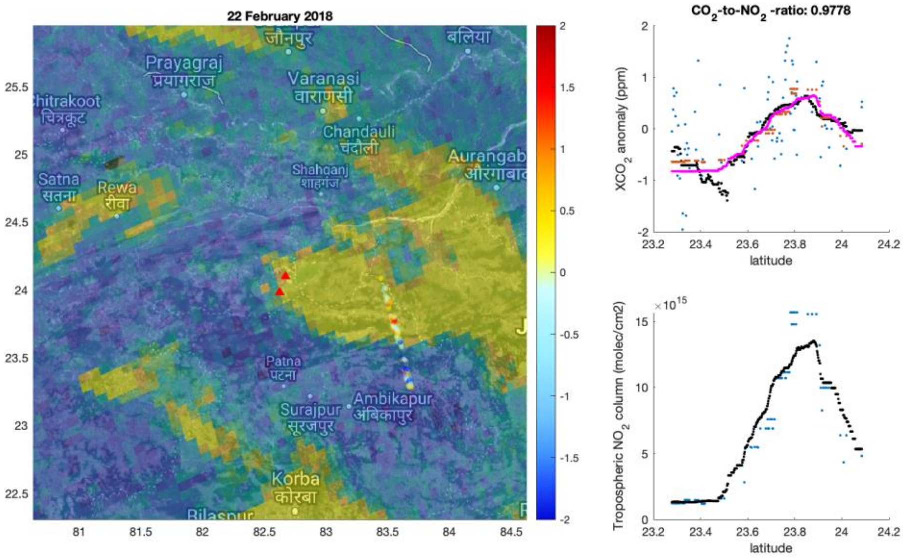

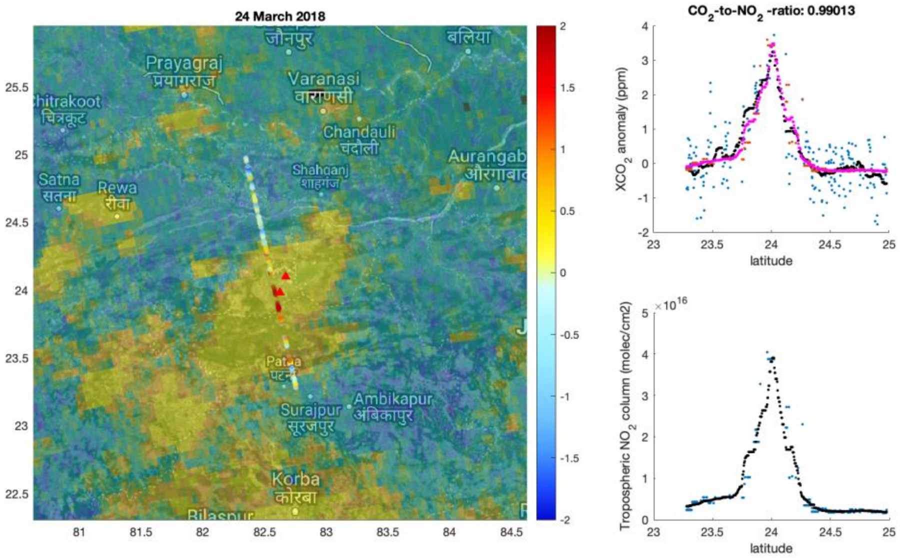

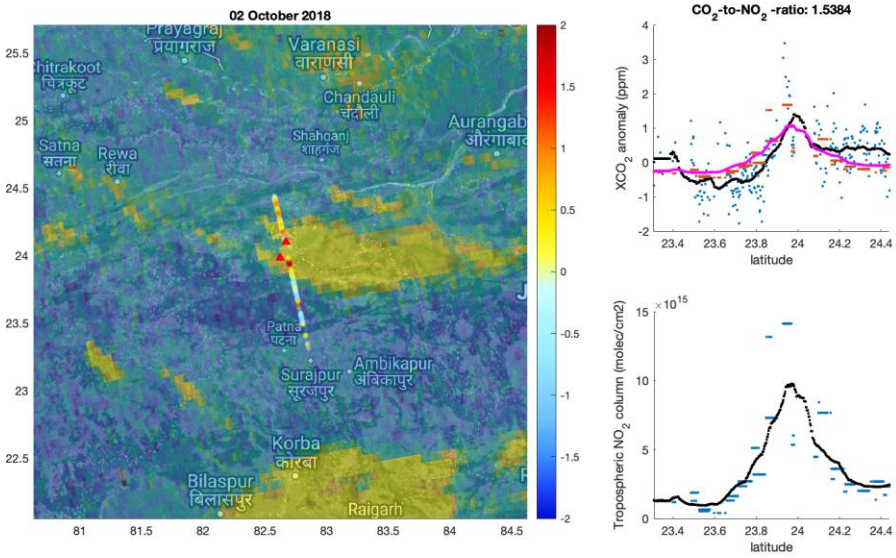

02 October 2018
Prayagraj
प्रयागराज
Varanasi
वाराणसी
Chitrakoot
चित्रकूट
Chandauli
चंदौली
Satna
सतना
Rewa
रीवा
Shahganj
शाहगंज
Aurangab
Patna
पटना
Ambikapur
अंबिकापुर
Surajpur
सूरजपुर
Korba
कोरबा
Bilaspur
बिलासपुर
Raigarh
CO$_2$-to-NO$_2$ -ratio: 1.5384
XCO$_2$ anomaly (ppm)
latitude
Tropospheric NO$_2$ column (molec/cm2)
$\times 10^{15}$

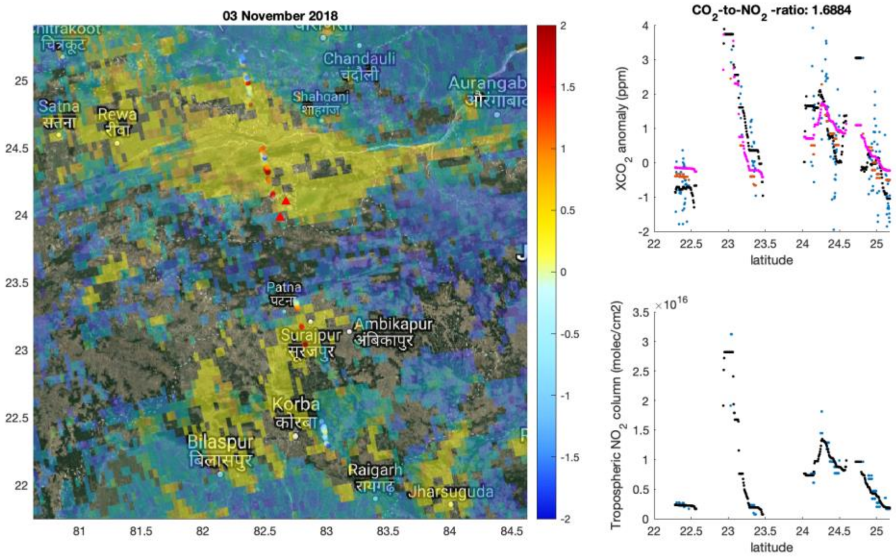

03 November 2018
Chitrakoot
चित्रकूट
Chandauli
चंदौली
Satna
सतना
Rewa
रीवा
Shahganj
शाहगंज
Aurangab
Patna
पटना
Ambikapur
अंबिकापुर
Surajpur
सूरजपुर
Korba
कोरबा
Bilaspur
बिलासपुर
Raigarh
रायगढ़
Jharsuguda
CO$_2$-to-NO$_2$ -ratio: 1.6884
XCO$_2$ anomaly (ppm)
latitude
Tropospheric NO$_2$ column (molec/cm2)
$\times 10^{16}$

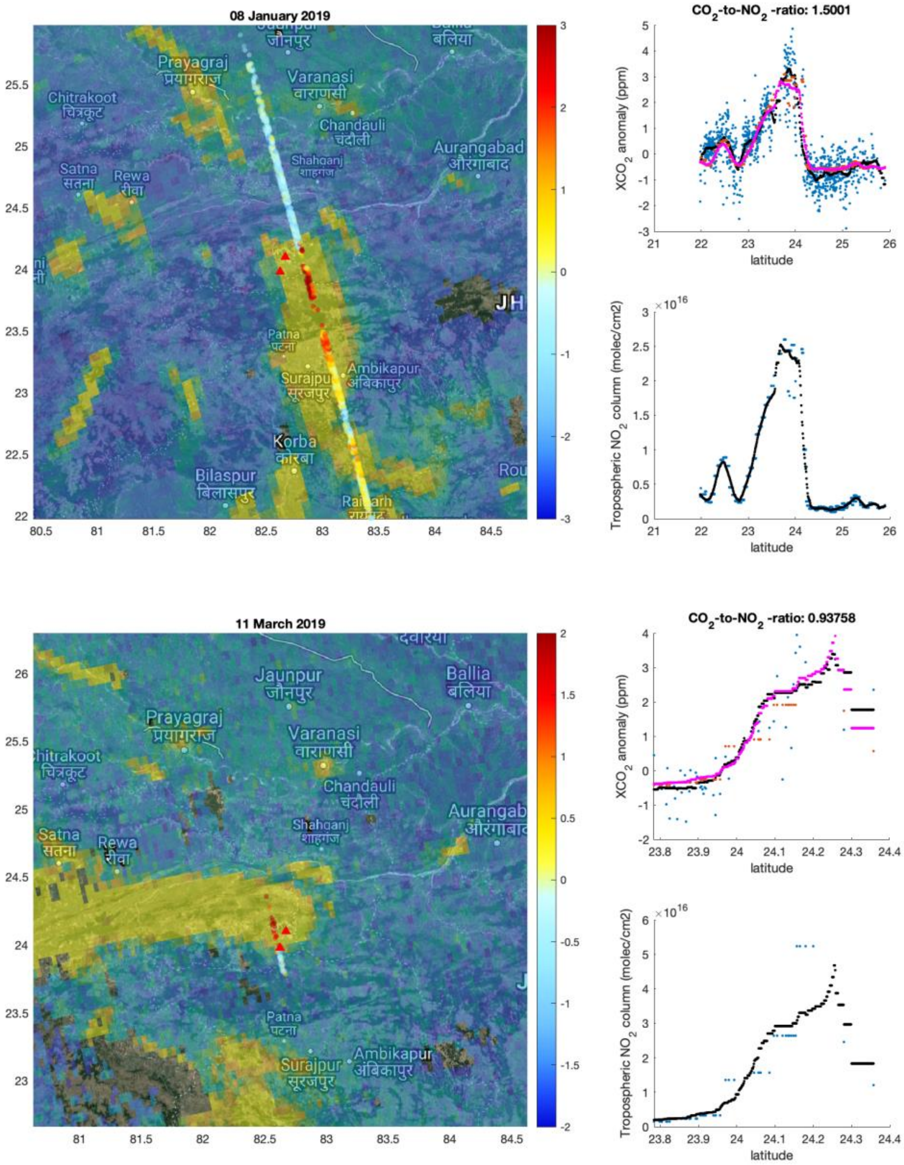

Figure 31 Examples of calculation of CO2-to-NO2 ratio using S5P tropospheric NO2 and OCO-2 XCO2 anomalies during several days (the dates are indicated on the top of the maps) over Sasan and Vindhyachal power stations in India. The panels on right site of the figure correspond to the tropospheric NO2 and XCO2 anomaly collocations as a function of latitude. The running means are indicated in black lines. We also apply linear regression to transform tropospheric NO2 to XCO2 (magenta for running mean and orange for individual points). The CO2-to-NO2 ratio is presented in the top right of the figure in units of 10^{-16} ppm/(molec/cm^2).

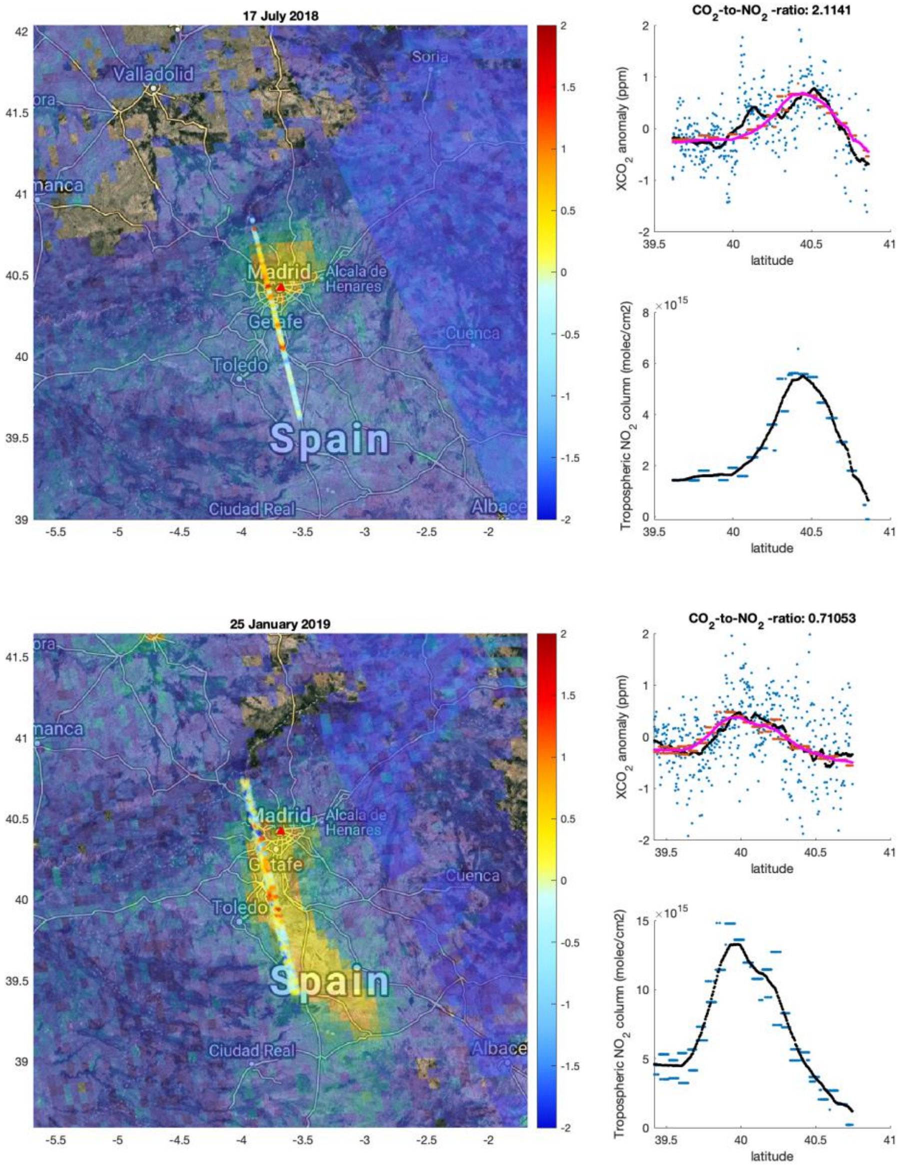
17 July 2018
CO2-to-NO2 -ratio: 2.1141
XCO2 anomaly (ppm)
latitude
Tropospheric NO2 column (molec/cm2)
Valladolid
Soria
Madrid
Alcala de Henares
Getafe
Toledo
Cuenca
Spain
Ciudad Real
Albace
25 January 2019
CO2-to-NO2 -ratio: 0.71053

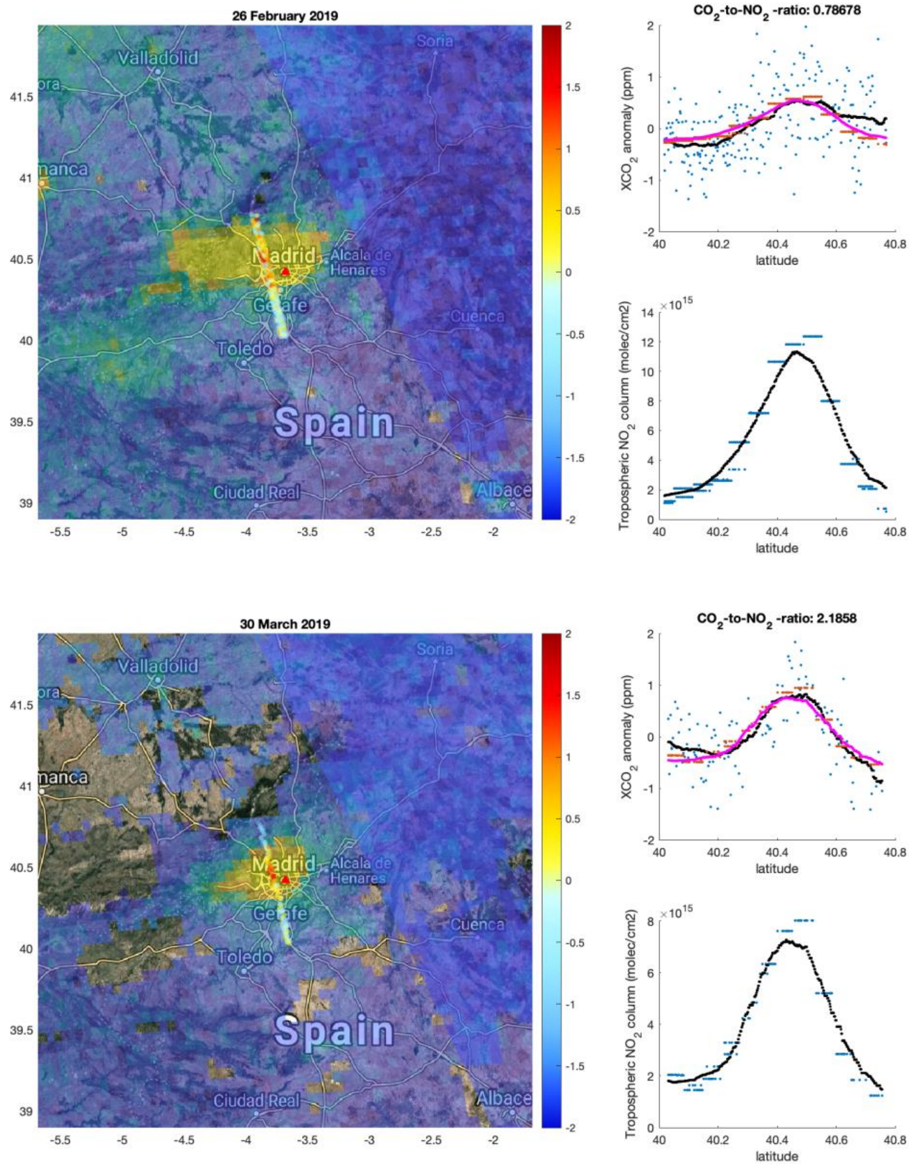

Figure 32 As Figure 31 but for Madrid.

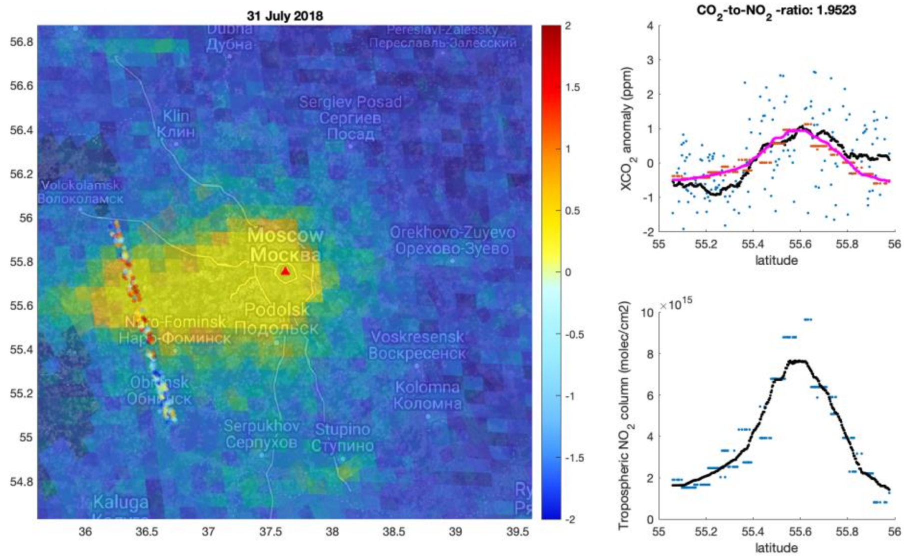

31 July 2018
Moscow
Москва
Podolsk
Подольск
Naro-Fominsk
Obninsk
Klin
Клин
Sergiev Posad
Сергиев
Посад
Volokolamsk
Волоколамск
Orekhovo-Zuyevo
Орехово-Зуево
Voskresensk
Воскресенск
Kolomna
Коломна
Serpukhov
Серпухов
Stupino
Ступино
Kaluga
Dubna
Дубна
Pereslavl-Zalessky
Переславль-Залесский
CO_2-to-NO_2 -ratio: 1.9523
XCO_2 anomaly (ppm)
latitude
Tropospheric NO_2 column (molec/cm2)
$\times 10^{15}$

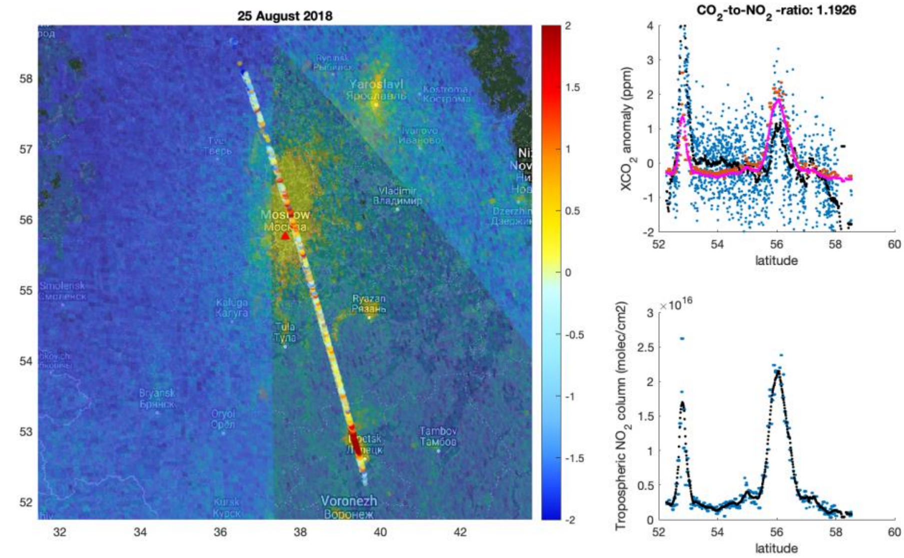

25 August 2018
Moscow
Москва
Yaroslavl
Ярославль
Vladimir
Владимир
Ryazan
Рязань
Kaluga
Калуга
Tula
Тула
Smolensk
Bryansk
Брянск
Oryol
Орёл
Tambov
Тамбов
Voronezh
Воронеж
Kursk
Курск
CO_2-to-NO_2 -ratio: 1.1926
XCO_2 anomaly (ppm)
latitude
Tropospheric NO_2 column (molec/cm2)
$\times 10^{16}$

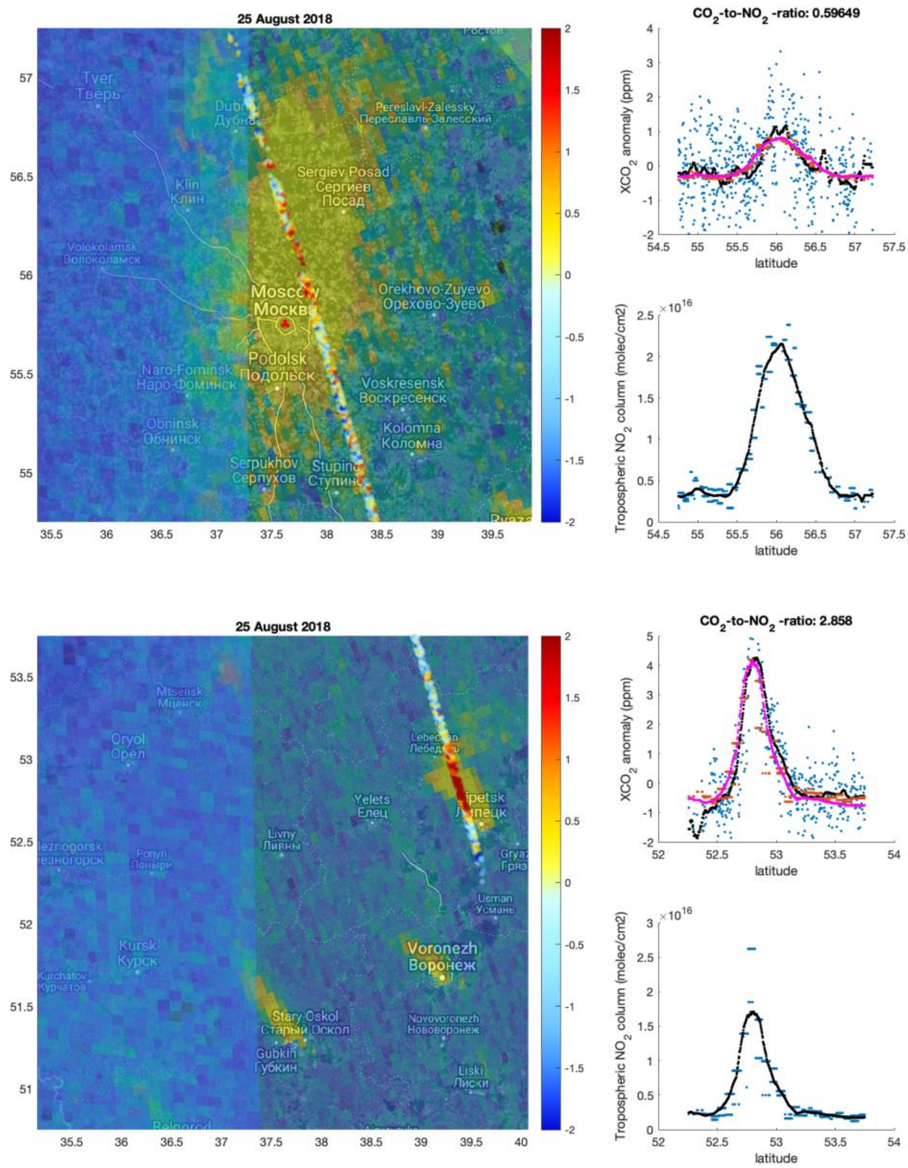

Figure 33 As Figure 31 but for Moskow.

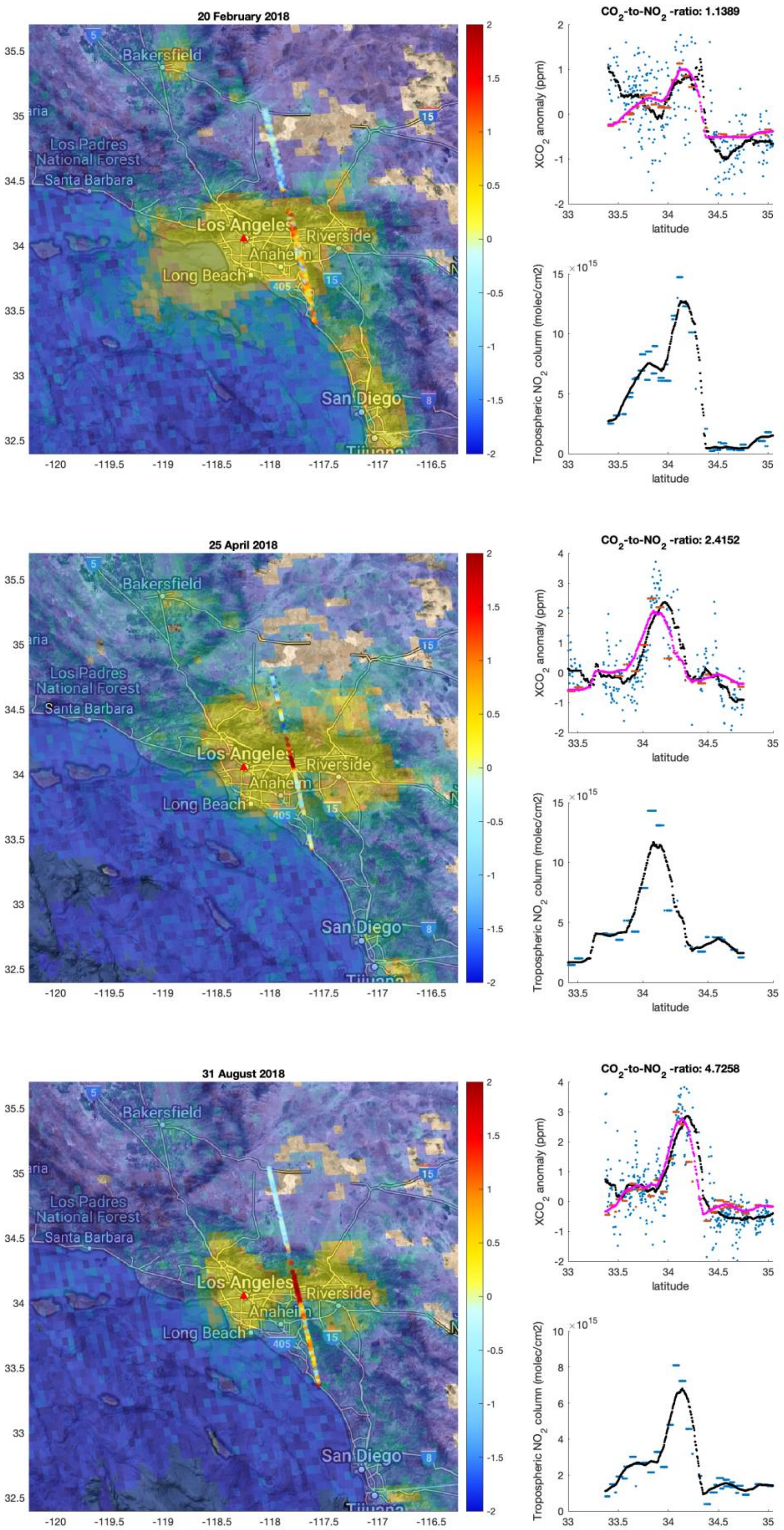
20 February 2018
CO2-to-NO2 -ratio: 1.1389
25 April 2018
CO2-to-NO2 -ratio: 2.4152
31 August 2018
CO2-to-NO2 -ratio: 4.7258
Bakersfield
Los Padres National Forest
Santa Barbara
Los Angeles
Riverside
Anaheim
Long Beach
San Diego
Tijuana
XCO2 anomaly (ppm)
Tropospheric NO2 column (molec/cm2)
latitude

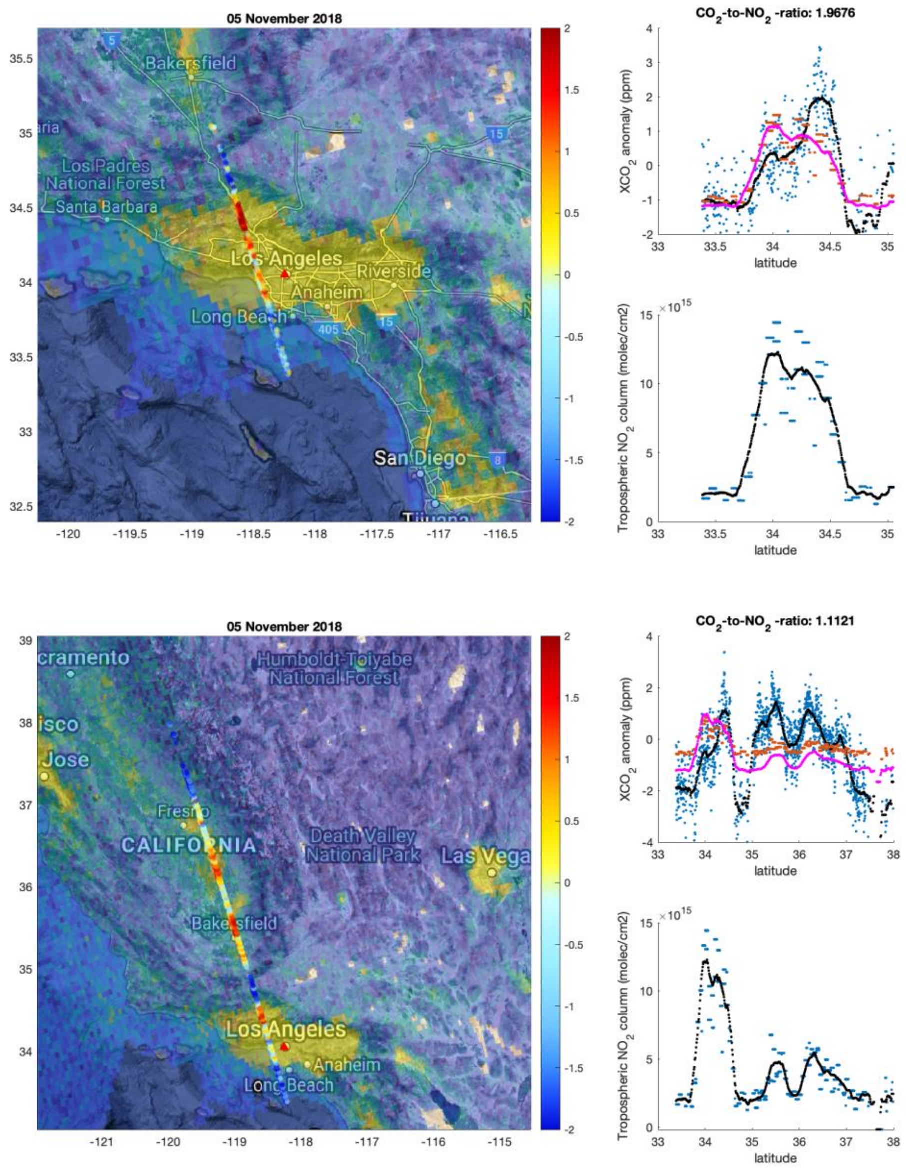

Figure 34 As Figure 31 but for Los Angeles.

2.2.3 Emission estimation

Once we identify the plumes using collocated OCO-2 and S5P observations we can try to estimate the CO2 emission from power plants and cities. Nassar et al. (2017) first estimated CO2 emissions using actual space-based XCO2 data. They studied the emission of six individual power plants using Gaussian plume model. Zheng et al. (2019) studied these same six power plants using WRF chemistry transport model. Recently, Reuter et al. (2019) used an approach similar to ours to detect OCO-2 overpasses over a few sources and to estimate cross-sectional flux of power plants and cities. We will test these different approaches here.

We also evaluate how to benefit from the S5P NO2 measurements since we have still limited amount of potential cases for estimating CO2 emissions directly from XCO2 data. Here, we focus on estimating the emissions of Matimba power station in South Africa. In this case study, during the period of one year, we have four potential cases for direct emission estimation. For the financial year 2016/17 the company maintaining the Matimba power station provided an estimation of the annual emissions of 28 Mt/yr. ODIAC 2017 emissions dataset report annual emission of about 26 Mt/yr. The company also reports the annual NOx emissions (as NO2) of about 77 kt/yr. This would indicate NOx/CO2 emission ratio of about 2.7×10^{-3}.

Cross-sectional flux

11 July 2018

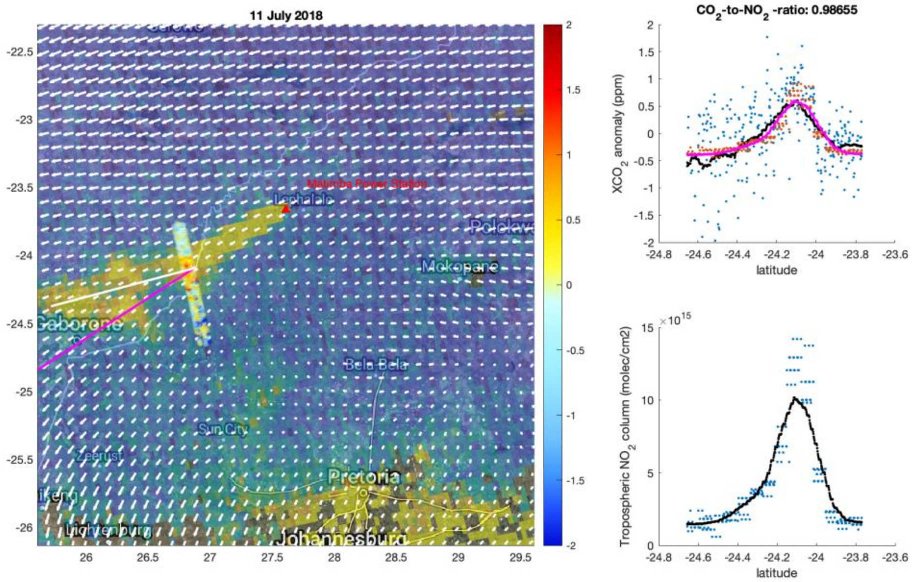

Figure 35 Illustration of cross-sectional flux using S5P tropospheric NO2 and OCO-2 XCO2 anomalies (the date is indicated on the top of the maps) over Matimba power station. The ECMWF 10m wind information are shown as white arrows. The magenta line indicates the direction of the plume (according to the ECMWF wind) and the white line indicates the wind direction perpendicular to the OCO-2 flight direction (needed for the emission calculation). The panels on right site of the figure correspond to the tropospheric NO2 and XCO2 anomaly collocations as a function of latitude. The running means are indicated in black lines. We also apply linear regression to transform tropospheric NO2 to XCO2 (magenta for running mean and orange for individual points). The CO2-to-NO2 ratio is presented in the top right of the figure in units of 10^{-16} ppm/(molec/cm^2).

Reuter et al. (2019) use a simple formula to infer the “cross-sectional flux”

$$E = 0.5\sqrt{\pi/\ln(2)} \times (M/A) \times C \times w \times FWHM \times a$$

In this formula M is the molar mass of CO2 (44.01 g/mol), A is Avogadro’s constant, C is the dry air column, w is the wind speed perpendicular to the OCO-2 flight direction, $FWHM$ is full width at half maximum (given by the Gaussian fit of the NO2 profile) and a is the amplitude of XCO2 in ppm. If we use typical value of 2.16×10^{25} molec/cm^2 for C, the formula becomes

$$E = 0.53 \times w \times FWHM \times a$$

Figure 35 shows an example of the plume from Matimba power station as well as the wind information needed for the emission calculation. Figure 36 illustrates the result of the Gaussian fit. The *FWHM* value is 20.1 km and the amplitude is 1.1 ppm. The normal wind speed is 1.2 m/s and we multiply this value by 1.4 as done by Reuter et al. (2019). The resulting flux is 19.4 Mt/yr, which is just a little smaller than the reported emission estimates (26-28 Mt/yr). Reuter et al. (2019) report the flux value of 31 Mt/yr, obtained with an higher normal wind speed (2.6 m/s). Using the same wind information produces the same results. This highlights the sensitivity of the emission estimate to the wind speed information. We note here, that the CO2-to-NO2 ratio (as described in the previous section) can also be derived by dividing the amplitude of CO2 by the amplitude of NO2. In this case, it gives the same value of about 1.

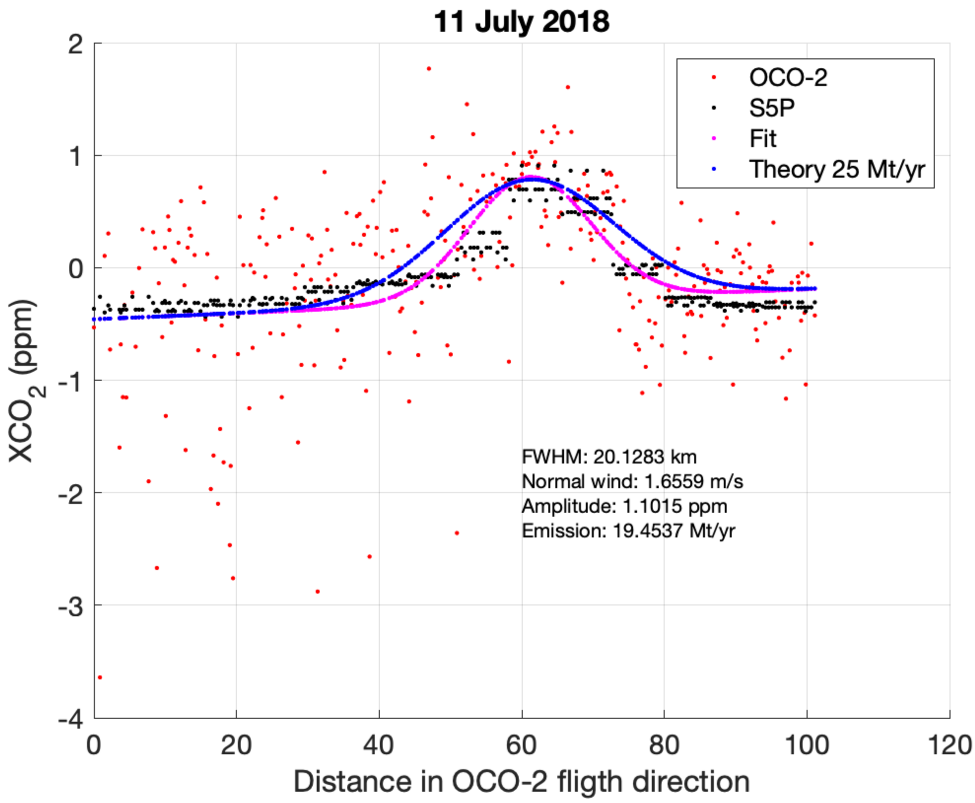

Figure 36 Illustration of the cross-track flux calculation over the Matimba power plant on 11 July 2018. Red dots indicate the XCO2 anomalies, black dots the S5P observation converted to XCO2 anomalies using linear regression, magenta dots the Gaussian fit and blue dots the theoretical Gaussian curve if the CO2 emission would be 25Mt/yr.

20 July 2018

We find that the *FWHM* is 31.4 km and the amplitude is 0.9 ppm. The normal wind speed is 1.7 m/s. The flux value is 26 Mt/yr. In this case, however, we corrected the wind direction (magenta versus white line in the map) as also done by Nassar et al. (2016) and Reuter et al. (2019). If we use the original ECMWF wind direction, the flux value will double. In this case it is not exactly clear what the wind direction should be.

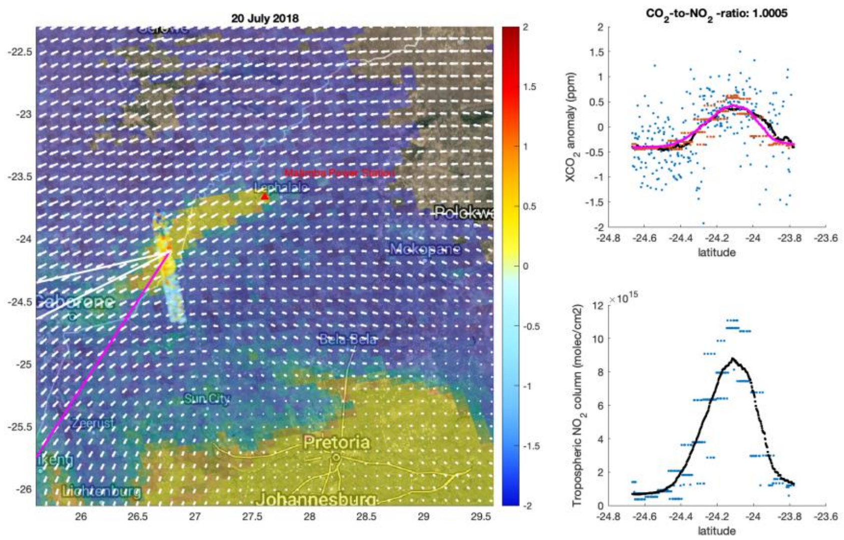

Figure 37 Same as Figure 35 but for 20 July 2018.

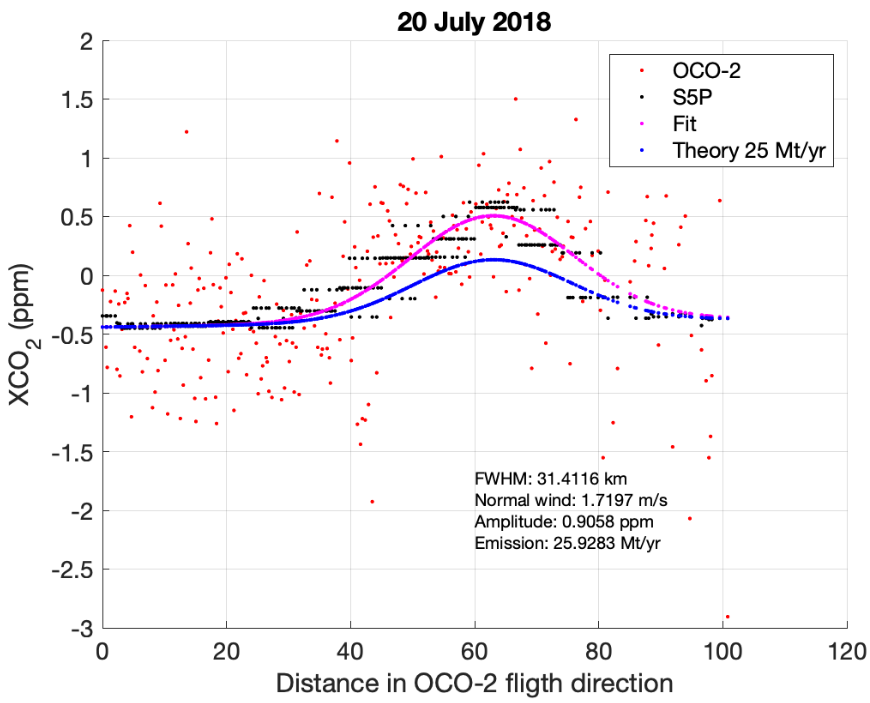

Figure 38 Same as Figure 36 but for 20 July 2018.

NOx emissions

An indirect way of deriving CO2 emission from point sources is to derive first NOx emissions from satellite observations (e.g. from OMI or TROPOMI) and then convert those into CO2 emissions, by using NOx-to-CO2 emission ratio.
NOx emissions from Matimba power plant have been derived here using OMI NO2 observations. We follow the method developed by Beirle et al., (2011) which is based on fitting the observations with a simple model that is a convolution between Gaussian function and exponential decay. Before applying the fitting technique, we also used the wind rotation technique as in Fioletov et al. (2015), in order to increase the amount of observations available for the fit. We first apply the wind rotation based on both u,v wind information and we then

calculate the linear density for the 1-D fit. One could also use a 2-D fitting model as done for SO2 by Fioletov et al. (2011).

Figure 39 show eight-month-average of tropospheric NO2 concentrations from OMI after applying the wind rotation to the same wind direction (from west to east). If we integrate the line densities perpendicular to the wind direction (i.e., on y axis, latitude) we obtain the line density are illustrated in the Figure 40 as a function of distance from source. In both figures we observe the density peak downwind from the source and an exponential decay after the peak. Fitting this with a gaussian-exponential model gives an emission value for NO2 of about 46 mol/s and a lifetime of about 4 hours. This gives annual NOx emission estimate about 60 kt/yr, quite close to the value 77 kt/yr reported by the company.

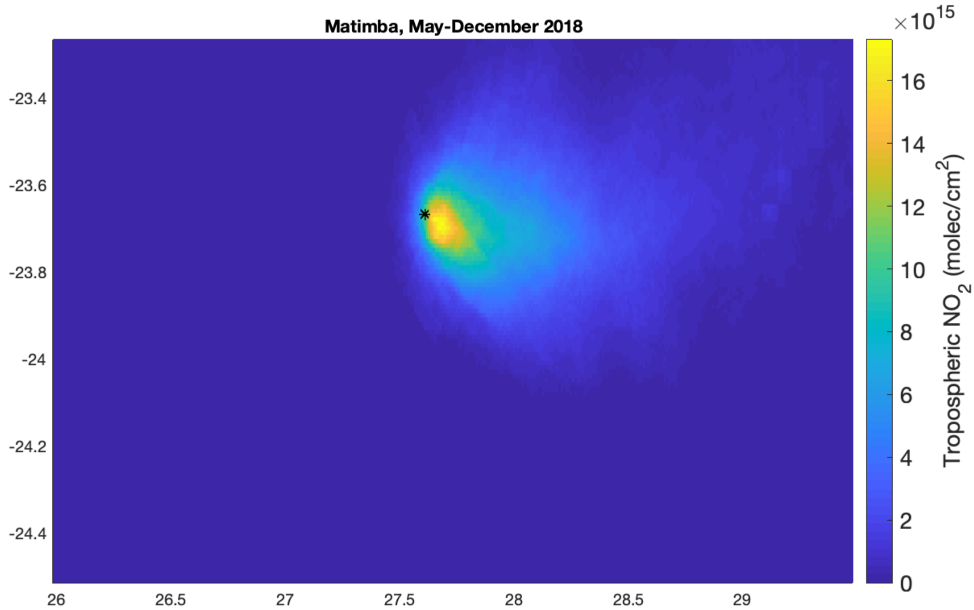

Figure 39 Average tropospheric NO2 columns from Matimba power station, May-December 2018. Wind speeds from 3 to 5 m/s. All plumes rotated to the same direction based on ECMWF 10 m wind fields.

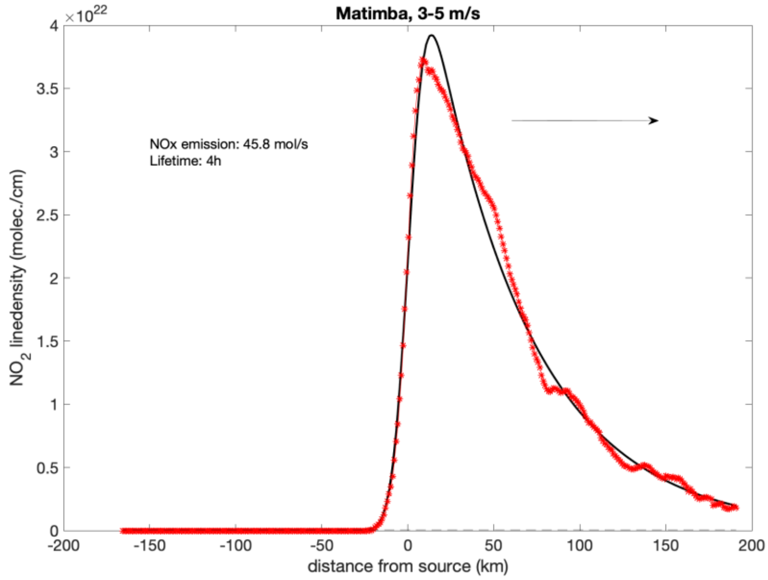

Figure 40 Average line densities from Matimba power station, May-December 2018.

Figure 41 illustrates the line densities for different wind speed ranges. We obtain NOx emission estimates between 45-48 mol/s and life times between 3-4h. Note that the values for range 3-5 m/s have changed slightly from the previous picture as we included a longer tail downwind from the source.

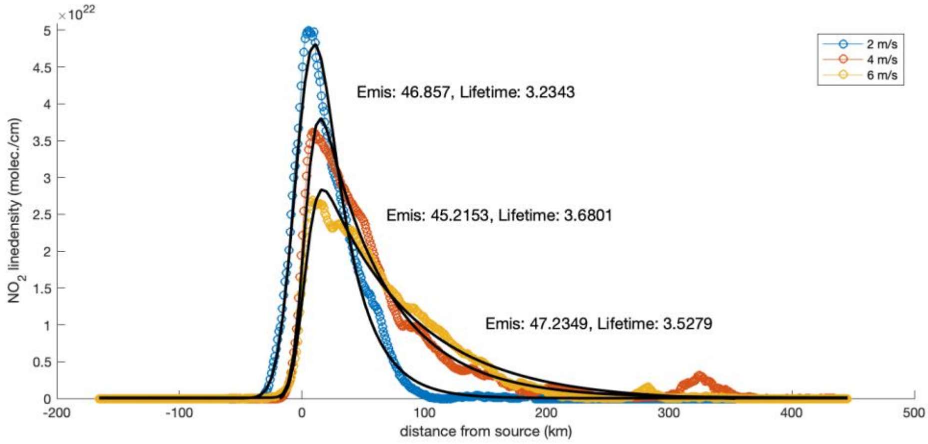

Figure 41 NO2 line densities for different wind ranges: 1-3m/s, 3-5 m/s, and 5-7 m/s.

Figure 42 below illustrates monthly line densities from May 2018 to December 2018 with wind speed in the range 3-5 m/s. Figure 43 illustrates also the line densities from an individual day (20 July 2018). We observe similar emissions as in the averaged case, but the effective lifetime is much longer (about 7 hours). As these values are close to the reported values, it would also indicate similar NOx-to-CO2 emission ratio. These types of fitting can only be done for selected dates where the plume shape is at least roughly Gaussian.

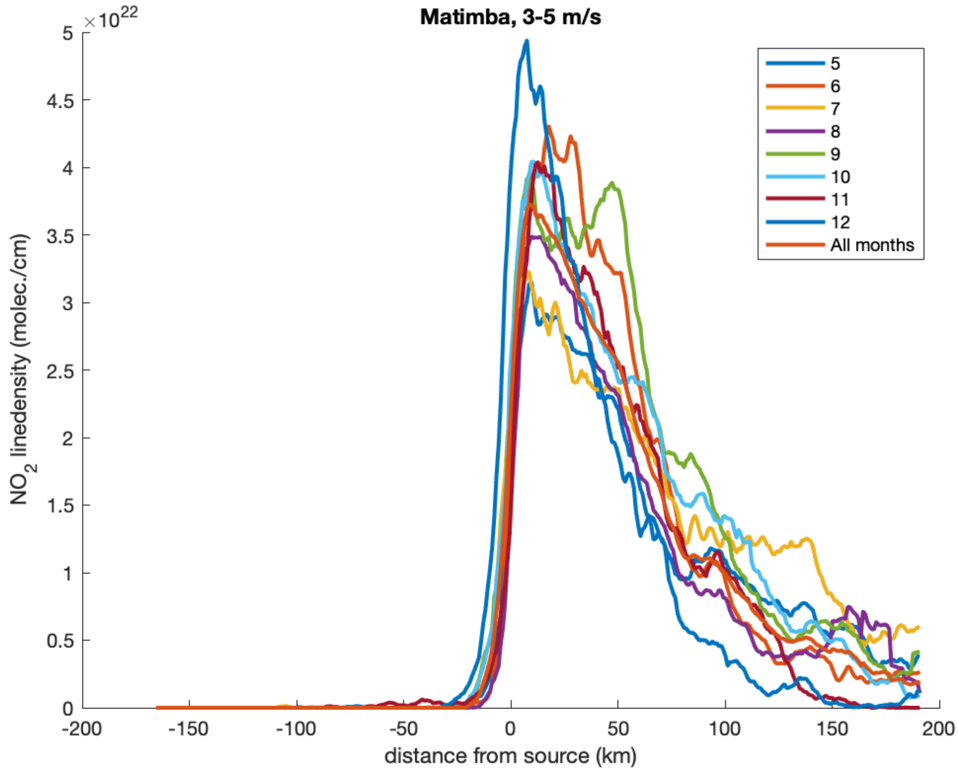

Figure 42 Monthly line densities of the plumes originating from Matimba power station.

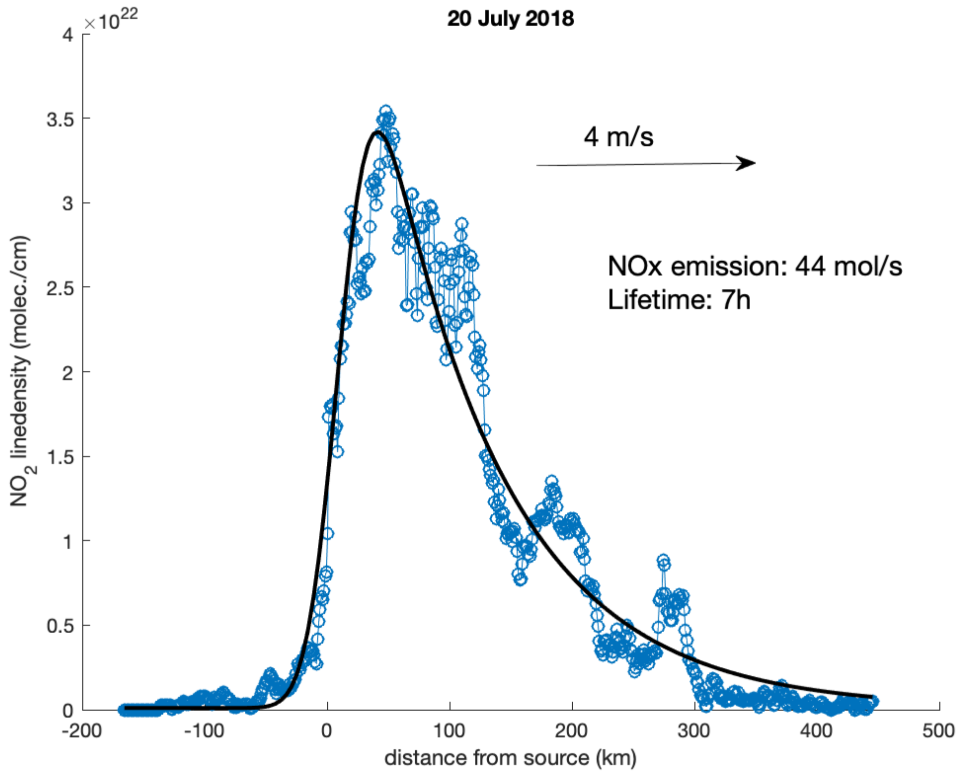

Figure 43 NO2 line density of an individual day 20 July 2018.

3 Societal application and user engagement

3.1 Method

The increasing availability of satellite-based atmospheric observations has increased the opportunities to employ such observations in practical applications for non-academic users or in multi-disciplinary studies outside of atmospheric research. The activities of WP3 focus on societal applications of atmospheric satellite-observations and users' engagement. We have collected input and needs from different types of users, from both the public and private sectors. We analyse different fields of applications, ranging from emission regulation monitoring for environmental authorities, supporting clean tech and green economy and their environmental sustainability efforts as well as multi-disciplinary socio-economical studies. We inform and educate different type of users on the potential and limitations of satellite observations for specific applications. The methods of interaction also vary based on the user type, including ad hoc meetings, reporting and consulting services customized to the specific user needs, demo audio and video material and iterative feedback process. Most of the applications included OMI and TROPOMI NO2 and SO2 satellite-based observations as indication of polluting emission combined to auxiliary data, since the current satellite-based CO2 retrievals had not the spatio-temporal coverage needed to monitor the areas of interest. Almost every user showed their interest in using space-based CO2 (in addition to short-lived gases) observations for similar applications, such as monitoring CO2 emission reduction. Future greenhouse gas missions with wider spatial coverage will improve the capabilities of monitoring man-made CO2 emissions and of providing user-driven solutions to achieve sustainable development goals.

In the following sections, we provide some examples of such applications including the use of satellite-based atmospheric observations.

3.2 Emission reduction verification from metal smelters

We analysed the SO2 emissions produced in the metal (mainly copper) smelting process from several plants operated by the Finnish clean tech company Outotec Oy. Satellite-based OMI SO2 columns and annual emission estimates based on such data (Fioletov et al., 2016) have been used to verify the emission reduction after the implementation of a sulfuric acid plant, designed to transform the gaseous SO2 into sulfuric acid. We tested several smelters at different locations and we found strong emission reductions just after the implementation of the sulfur-removing plant. The images and results achieved in the study were included in the company's sustainability report for 2018 (Outotec 2018) as well as published as scientific publication (Ialongo et al. 2018). As an example, Figure 44 (upper panel) shows the mean SO2 total columns from the OMI SO2 L3 product for 2014 and 2016 over Tsumeb (Namibia) copper smelter. In 2014, the SO2 concentrations reached their peak at around 0.1 DU over Tsumeb, while the SO2 levels decreased dramatically in 2016. , Figure 44 (central panel) shows the time series of the annual SO2 emissions obtained from the OMI-based catalogue (blue solid line). The error bars in Figure 44 indicate 2 standard deviations from the annual mean derived from OMI-based emission catalogue. The SO2 emission estimates from the Wood&Mackenzie Copper Smelter database (blue dashed line in Figure 44 - central panel) show values quite close to the OMI catalogue and similar year-to-year variability.

Furthermore, we planned and carried on several meetings to identify new applications and we found several case studies with similar emission reductions observed. For example, we analysed the Bor sulfuric acid plant in Serbia in order to evaluate whether the plant was functioning properly. The OMI-based SO2 emission time series show a rapid decrease of the emission since the installation of the sulfur-removing plant until 2018 (Figure 45, bottom panel). The company had the impression though that some of the smelter's gases were not directed to the plant (and hence there should be more SO2 emissions). OMI SO2 total column maps do not show a clear enhancement over the smelter in 2019 (Figure 45), but there was an increase in the noise level in the area. The emission for the year 2019 will be included in the analysis when available.

In addition, we analysed some cases related to CO2 emissions from ferrochrome production in South Africa. The sites of the plant are shown in Figure 46 over a map of CO2 emissions from the ODIAC database. As ferrochrome production is essentially a carbothermic reduction these plants produce very little NO2, which makes the collocated plume detection impossible. We found indeed that the ferrochrome plants are not visible in TROPOMI NO2 maps (we tested six plants with different technology). While we were able to locate many OCO-2 overpasses with XCO2 enhancements over these ferrochrome plants, we could not separate the contribution of the ferrochrome plants from the other emission sources in the area. Other cases will be tested in the future.

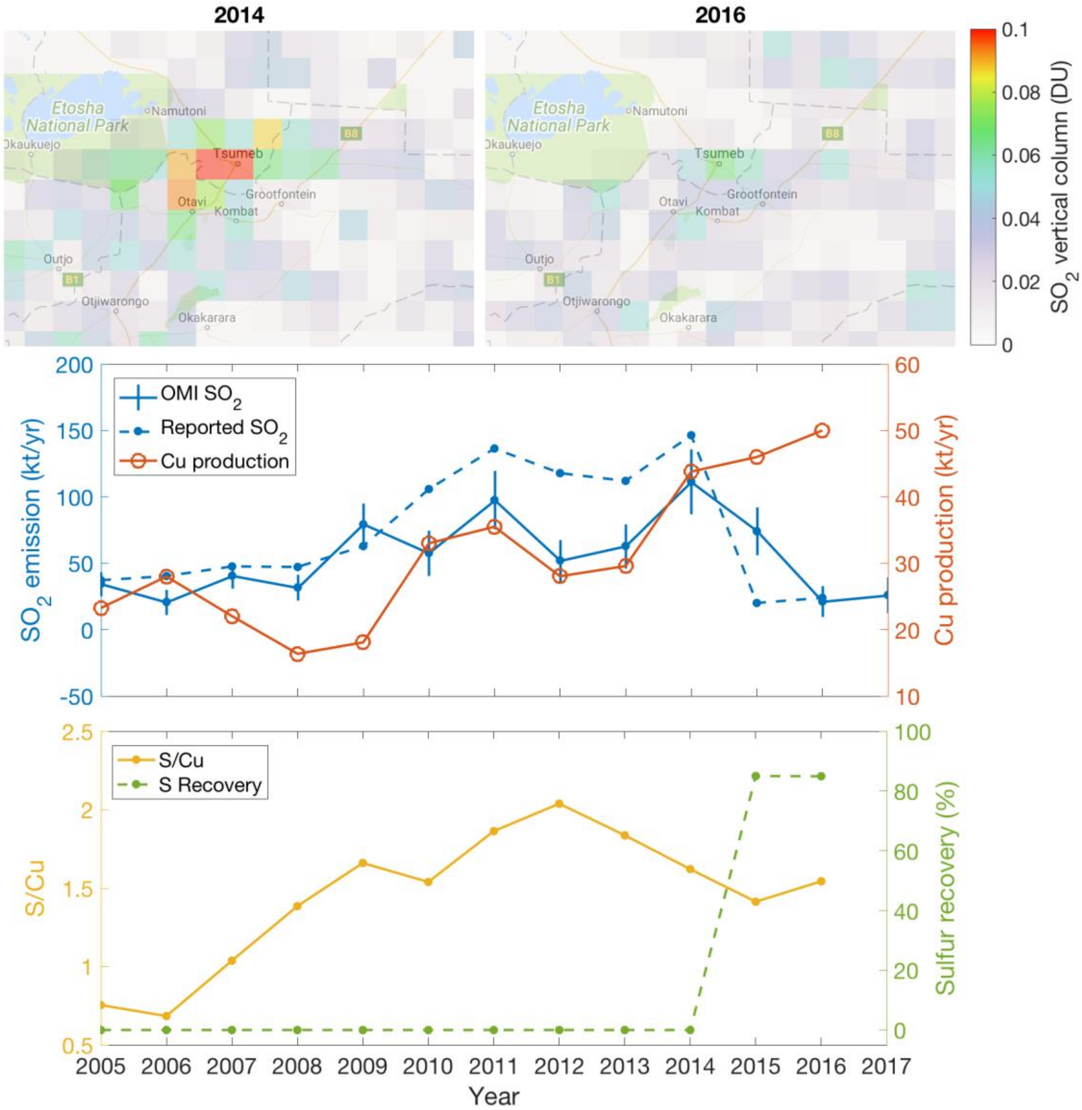

Figure 44 SO2 levels from copper smelter in Tsumeb (Namibia). Upper panel: SO2 total columns during 2014 (peak year) and 2016 from OMI SO2 L3 product. Central panel: SO2 emissions from OMI-based catalogue (blue solid line) and from Wood&Mackenzie database (blue dashed line). The error bars represent 2 standard deviations from the annual mean derived from OMI-based emission catalogue. The copper smelter production is shown with a red line. Lower panel: sulfur-to-copper ratio (yellow solid line) and sulfur recovery (green dashed line).

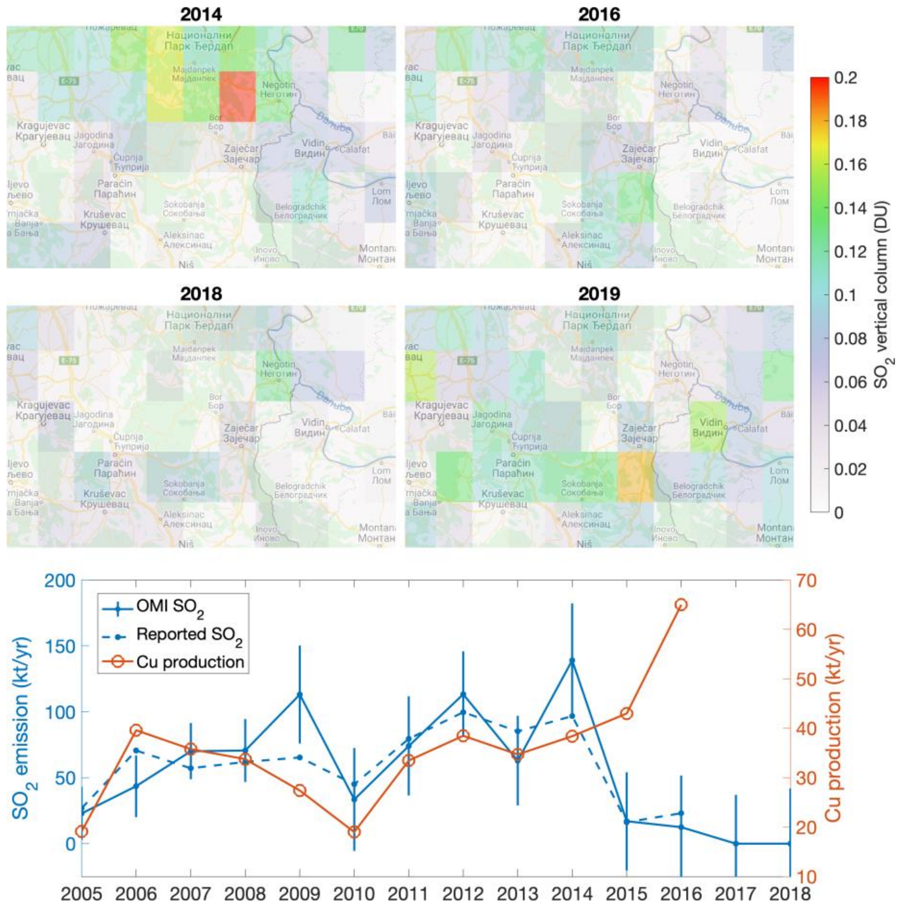

Figure 45 SO2 levels from copper smelter in Bor (Serbia). Upper and middle panels: Annual mean of OMI SO2 total columns over Bor metal smelter for 2014, 2016, 2018 and 2019. Lower panel: OMI-based annual SO2 emission time series from 2005 to 2018 from Bor smelter.

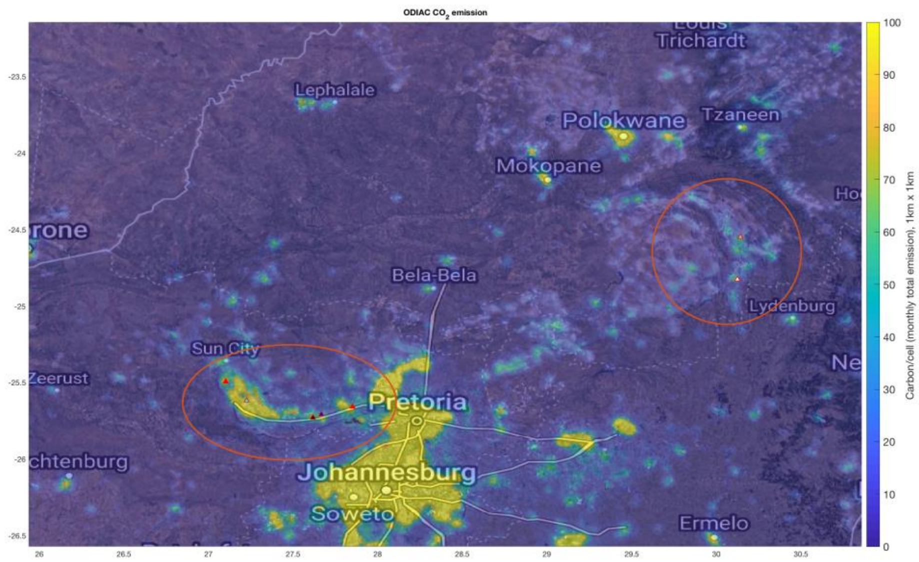

Figure 46 ODIAC CO2 emissions over South Africa. Triangle indicates the location of the Outotec ferrochrome plants.

3.3 Satellite-based air pollution observations for environmental authorities

We collaborated with the Finnish Ministry of Environment to provide new information on the potential of satellite-based observations for air pollution monitoring in Finland and neighboring countries. We produced an extensive report (in Finnish) including high resolution maps over Finland and in the surrounding areas (see e.g. Figure 47) based on TROPOMI NO2 tropospheric columns in order to demonstrate the capability of satellite data in monitoring air pollution. We produced also high-resolution maps for several Finnish cities. Figure 47 shows how the new high-resolution observations from TROPOMI are able to detect the main urban areas in Finland as well as the main traffic lanes from Helsinki to other cities such as Tampere, Turku and Lahti with much higher accuracy. For example, a much smaller NO2 signal is detected in the Helsinki-Turku direction, compared for example to the Helsinki-Tampere direction, where the amount of vehicles in transit is on average much higher. Also, the main connection to the Russian border from Mikkeli to Lappeenranta (with a large contribution of heavy vehicle traffic) is easily detectable from the map.

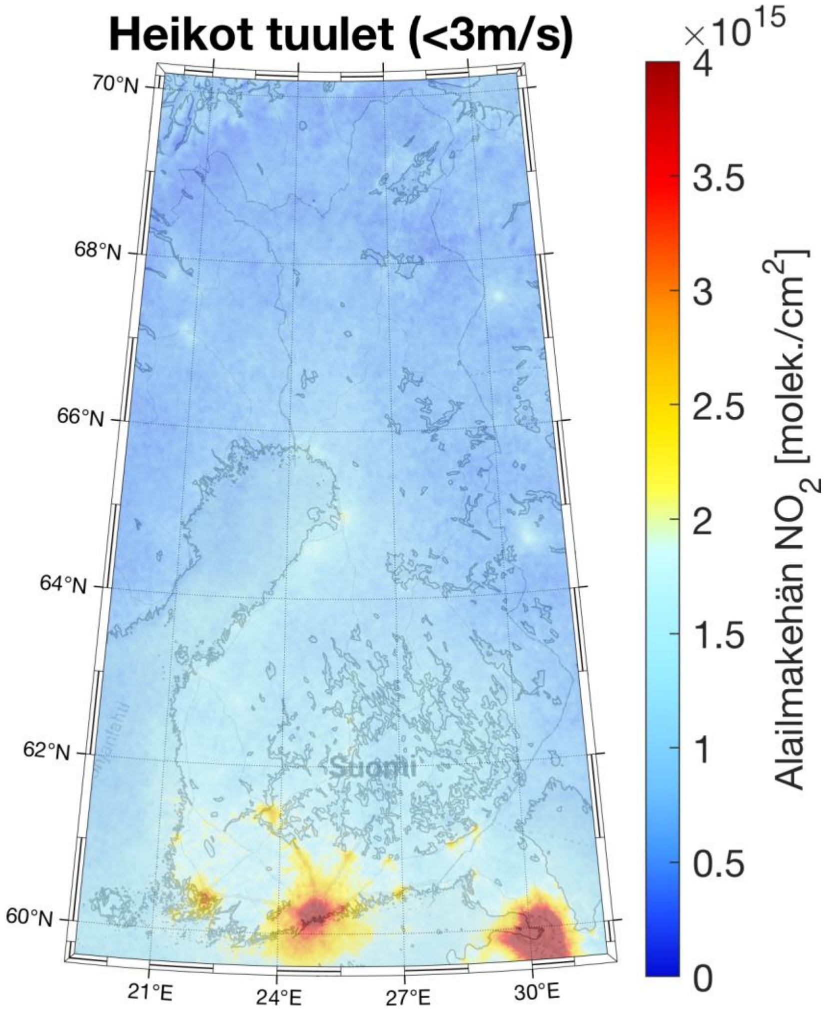

Figure 47 TROPOMI NO2 tropospheric columns over Finland during the period 1.5.2018-31.08.2019 under calm wind conditions (wind speed below 3 m/s) as included in the report to the Finnish Ministry of Environment.

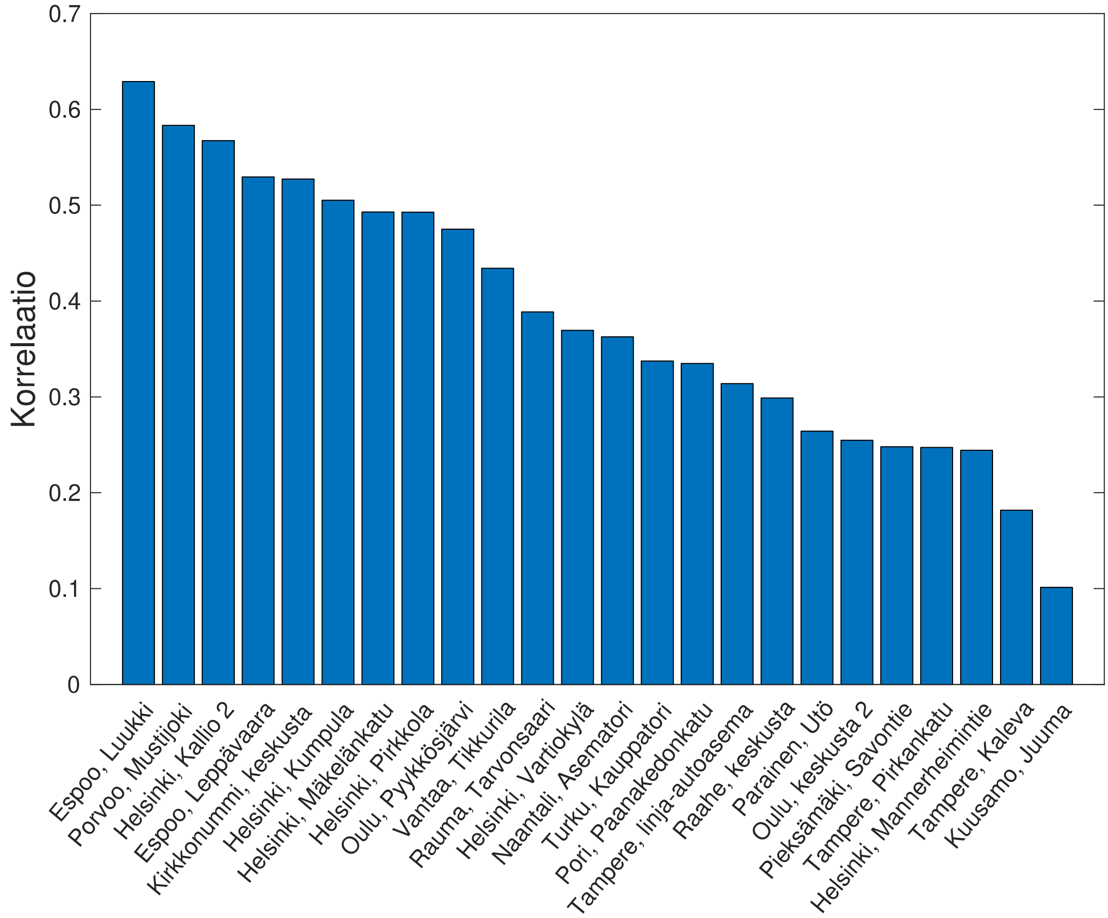

Figure 48 Correlation coefficient between TROPOMI NO2 tropospheric columns and in situ surface concentrations measured at Finnish AQ stations.

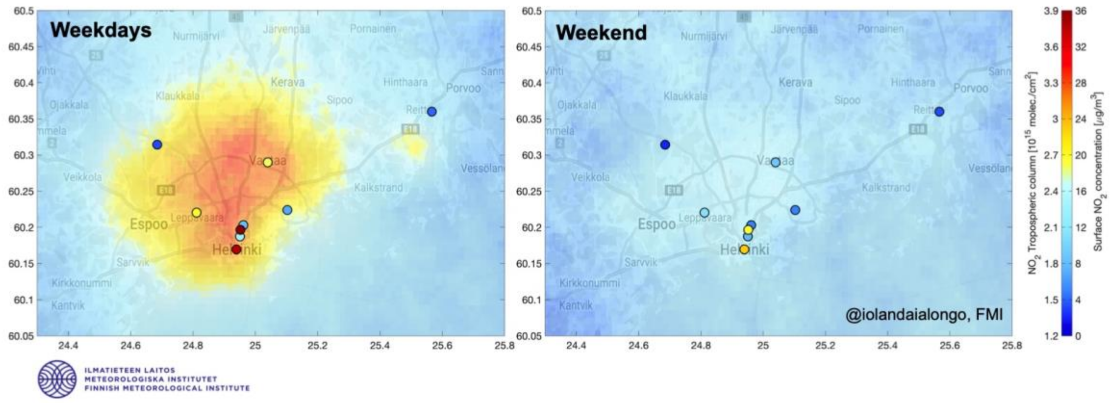

Figure 49 Average NO2 surface concentration (colored circles) and TROPOMI tropospheric NO2 over Helsinki during the period 1.5.2018-31.08.2019 for the weekdays (left) and weekends (right).

In addition, we evaluated the correlation between TROPOMI NO2 columns and in situ NO2 surface concentrations measured in Finland and in other major cities in Europe. The correlation values for each AQ station in Finland are shown in Figure 48. The best correlation was found with AQ stations with small temporal variability in the pollution levels, which correspond to most of the background stations. When comparing the mean NO2 levels for different cities in Finland and in Europe the correlation between satellite- and in situ measurements from the AQ stations in the city centers is high. Figure 49 shows the average NO2 spatial distribution from satellite- and surface measurements in Helsinki. We note how

TROPOMI NO2 columns are sensitive to changes in the polluting emissions occurring at the surface, such as the reduction in polluting emissions due to the reduced commuter traffic during the weekend (Figure 49, right panel), compared to working days (Figure 49, left panel). A similar reduction is also visible from the in situ NO2 measurements (filled circles in Figure 49). We conclude that TROPOMI NO2 observations are consistent with in situ measurements and can complement the traditional network for urban air quality monitoring in Finland.

We also carried on a more quantitative validation of TROPOMI NO2 products using Pandora observations in Helsinki (see also Sect.3.7). In general, we find that TROPOMI NO2 total (summed) columns in Helsinki are smaller than Pandora total columns for relatively high concentrations, while low values are overestimated. We find this partially related to the relatively coarse TM5-MP model profile shapes used in the TROPOMI retrieval to compute the tropospheric air-mass factors and thus the tropospheric vertical columns. We note how the both satellite- and ground-based datasets show a very similar temporal variability, with NO2 peaks occurring during the same days. The largest differences between TROPOMI and Pandora vertical columns, with TROPOMI smaller than Pandora, correspond to relatively high NO_2 enhancements. This is expected, as the comparatively large size of the TROPOMI pixels leads to greater spatial averaging compared to the Pandora field of view.
Nevertheless, the observed differences are within the target uncertainty for TROPOMI NO2 retrievals. One remaining issue is related to the fact that TROPOMI produces NO2 tropospheric columns, which are relatively high overall in Finland compared to similar latitudes (Sweden for example), especially in the background. This problem might be related to an overestimation of the stratospheric column or other issues related to the surface albedo input. Further investigations are needed in order to understand this issue. Upcoming versions of the NO2 retrieval algorithm will be tested as soon as available.

The results were presented as seminar at the Finnish Ministry of Environment and published as FMI report (https://helda.helsinki.fi/handle/10138/311906) and as scientific publication (Ialongo et al., 2020). The feedbacks were quite positive and several additional applications have been planned for 2020, including a potential involvement of local authorities at city level. Also, similar applications of future satellite-based CO2 observations are among the users' needs.

3.4 Satellite-based air pollution observations for corporate environmental sustainability in the energy sector

We analysed the level of polluting emission from oil refinery maintained by the Finnish company Neste Oy in the Kilpilahti industrial area in Porvoo, Finland (about 40 km east of Helsinki). We were able to detect the NO2 signal using oversampled maps of TROPOMI NO2 tropospheric columns over the refinery (see the NO2 enhancement about 40 km east of Helsinki in Figure 50). The quantitative estimation of emission is challenging because the refinery is located close to the city of Helsinki and the contribution from the capital region and emissions from traffic tend to dominate the NO2 patterns.

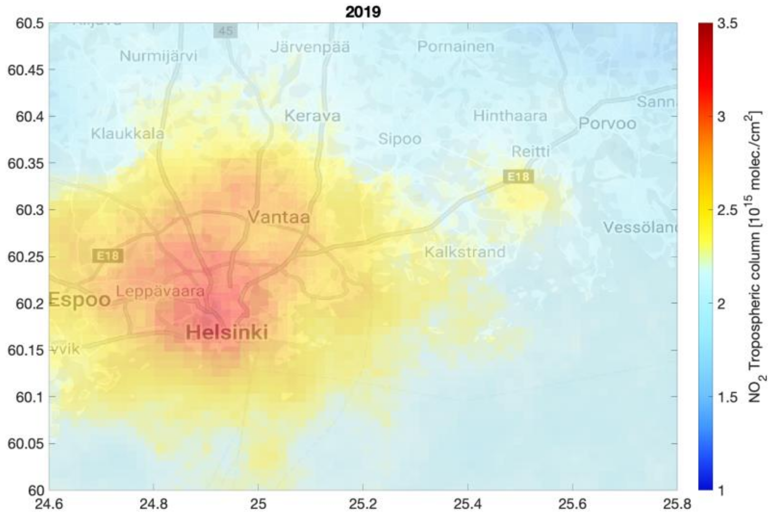

Figure 50 TROPOMI tropospheric NO2 columns over Helsinki and Kilpilahti industrial area in Porvoo (Finland) where NESTE oil refineries are located. The data are gridded using an oversampling method on a 1x1 km grid and over one year time range (2019).

We also used OMI observations over the refineries to analyse the changes in NO2 levels since year 2005. We find similar decreasing NO2 levels from both satellite- and ground-based in situ NO2 measurements over the Kilpilahti industrial area. We note again that the relatively coarse pixel size of OMI does not allow for a complete separation between the contribution from the traffic from Helsinki area (located only 40 km West from the refineries) and the refinery itself (generally smaller). Both TROPOMI NO2 maps (Figure 50) and OMI-based time series (Figure 51) have been included in the company sustainability report for 2018 and 2019. Monitoring polluting emissions from Kilpilahti industrial area is also of interest for and reported to the City of Porvoo environmental authorities. Finally, we point out that there would be interest by the company to use satellite-based CO2 observations similarly to short-lived gases but the currently available instruments are not yet able to provide the required spatial coverage.

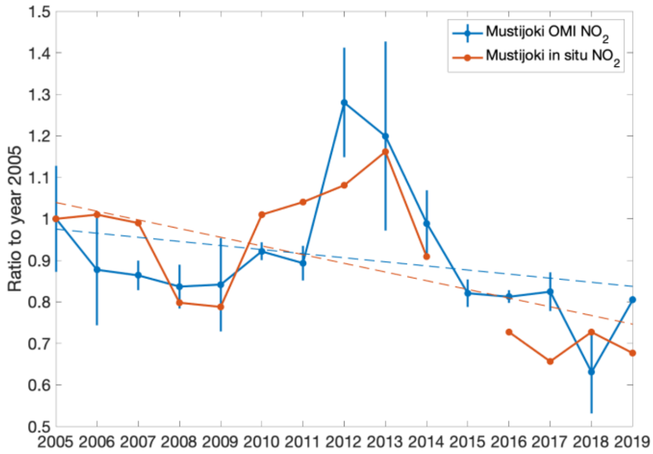

Figure 51 Time series of in situ NO2 concentration (black line) from Mustijoki air quality station and TROPOMI tropospheric NO2 columns (blue line) over Kilpilahti area in Porvoo (Finland) where NESTE oil refineries are located. The data are normalised to the 2005 values.

3.5 Satellite-based atmospheric observations for monitoring emissions from the energy sector: scientific collaboration with RED research platform at the Lappeenranta University of Technology

We collaborated with the RED (Revealing emission discrepancies) platform from the Lappeenranta University of Technology, that aims a evaluating existing polluting emission inventories. The platform combines different fields of expertise, including atmospheric monitoring as well as evaluating the impact of business and industry on the environment. In particular, we provide our expertise in satellite data and their applications to provide information on polluting emissions. J. Hakkarainen is supervising a master thesis with focus on the case study of the Bełchatów Power Station in Poland.

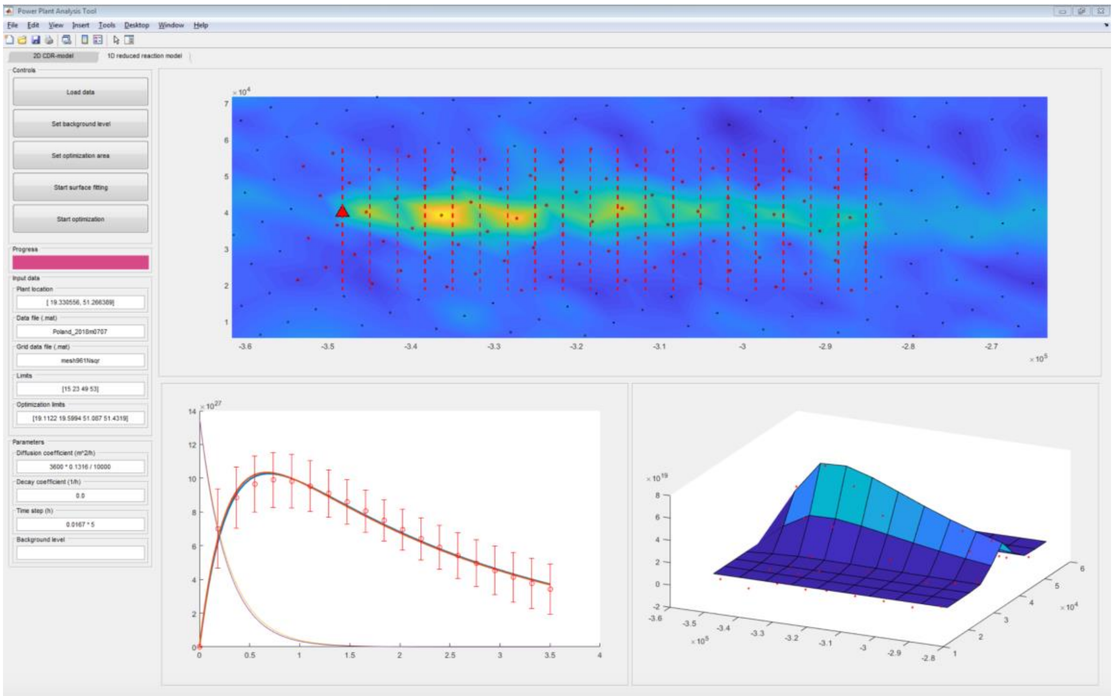

Figure 52 Graphical user interface created in the MSc project of Teemu Härkönen. Plume originating from Bełchatów Power Station in Poland. The values estimated were generally lower than the values reported by the European Pollutant Release and Transfer Register.

In the MSc work two 'physics-based' approaches were considered for the emission estimation of nitrogen oxides during individual days in 2018. Bełchatów coal power station in Poland was selected as a case study because it is the single highest producer of nitrogen oxides (NOx), carbon dioxide (CO2), and sulphur dioxide (SO2) emissions in Europe. In addition, the Energy department at LUT University has connections to the operating company. Figure 52 presents a graphical user interface of the software created in this project. The values obtained in this work were in general lower than the values reported by the European Pollutant Release and Transfer Register. This is in agreement with the results found also in the DACES project. The MSc thesis is available online (link).

3.6 Satellite-based atmospheric observations for socio-economical studies

We collaborated with the University of Helsinki - Russian Digital Studies of the department of Social science. We hosted Dr Nadya Stepanova from Univ. of Yakutsk (Russia) and we worked together on developing approached to include satellite-based air pollution and land-use data into socio-economical studies. In particular we focused on the connection between changes in economic policies and environmental parameters over sparsely populated regions (in this case the region of Yakutia, Russia). The funding for the visit was successfully obtained from the Academy of Finland. We combined the socio-economical data (e.g., population, public and private investment, energy production, industrial production) in Yakutsia with TROPOMI NO2 observations and we analysed several case studies such as emissions from gold, diamond and coal mining, as well as energy production and their connection to public investment and revenues.

For example, we found a reduction in NO2 concentrations in the municipal district of Neryungry (Southern Yakutia) from 2018 to 2019 using oversampled TROPOMI NO2 maps (Figure 53). We investigated the reasons for such reduction by using official documentation from the authorities and companies operating in the area. This decrease was explained by a small reduction in energy and heat production from the Neryungri power station (NPS) as well as a little decrease in coal consumption. These changes are possibly related to the construction of power cable lines since the beginning of 2019, which allowed the FEGC (Far East Generating Company), the main energy producer in South Yakutia, to supply the energy produced by the Neryungri power station into the wholesale market of energy (which includes other generating plants operating on gas and hydro power). This opens the opportunity for big local consumers (such as Mechel Company, owner of YakutUgol-Nerungrinsky coal mine), to purchase from other energy providers and therefore reduce the demand for the NPS. Also, winter season 2019 was warmer than 2018, which reduced the need for heating in the area. Finally, part of this reduction can be explained by the modernization of Denisovsky and Inaglinsky mines, where collectors were installed to remove most of the air polluting emissions from coal generation.

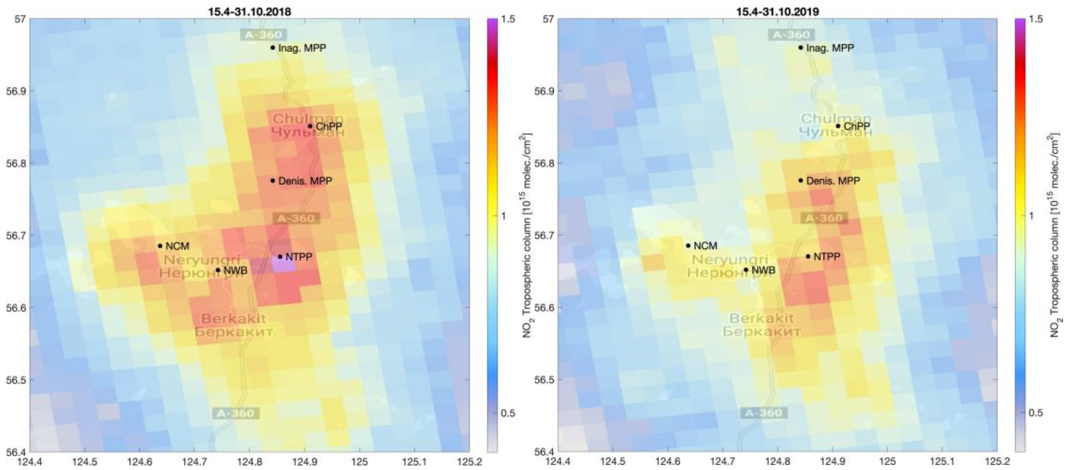

Figure 53 TROPOMI NO2 tropospheric columns over Neryungri in 2018 and 2019 (left and right, respectively). Black dots indicate the location of the major energy production sites and coal mines.

3.7 Other research activities

In preparation to the comparison between TROPOMI NO2 and XCO2 anomalies, we carried on TROPOMI NO2 validation study in Helsinki within the Sentinel 5P/TROPOMI validation team activities. The results found high correlation (r about 0.7) between satellite-based retrievals and ground-based observations from Pandora spectrometer. On average, TROPOMI total columns underestimate ground-based observations for relatively large Pandora NO2 total columns, corresponding to episodes of relatively elevated pollution. This is expected because of the relatively large size of the TROPOMI ground pixel (3.5 × 7 km) and the a priori used in the retrieval compared to the relatively small field-of-view of the Pandora instrument. On the other hand, TROPOMI slightly overestimates relatively small NO2 total columns. As an example, Figure 54 shows the scatterplot of Pandora and TROPOMI total columns over Helsinki (Finland). The weekend overpasses fall mostly into the bottom-left area of the scatterplot, corresponding to relatively small NO2 total columns from both Pandora and TROPOMI retrievals. This is expected due to the NO2 weekly cycle over urban

sites, i.e. reduced polluting emissions from traffic during the weekend compared to the weekdays. Furthermore, the overpasses corresponding to high wind speed values (green–yellow colours in Figure 54) also fall into the bottom-left area of the scatterplot. In these cases, the dilution by the wind acts to reduce the NO2 levels. Overall, the data points are quite close to the one-to-one line, except for some cases with elevated NO2 total columns measured by Pandora. These cases correspond to NO2 enhancements with small wind speed (below 3 m/s), when the spatial dilution effect of TROPOMI's ground footprint as compared to Pandora's narrow field of view is especially pronounced.
TROPOMI NO2 retrievals were also consistent with in situ surface observations in Helsinki and in Finland, overall. These results are published in the paper by Ialongo et al. 2020.
Furthermore, we contributed to a review study lead by NASA team (Duncan et al. 2019) focusing on space-based observations in the Arctic-Boreal Zone (ABZ). In, particular, we participated to the air pollution chapter with OMI and TROPOMI NO2 maps over Finland and with the evaluation of current satellite instruments to monitor air pollution at high latitudes. The paper provides also a set of recommendations and priorities for future missions concerning atmospheric monitoring as well as other relevant geophysical properties.

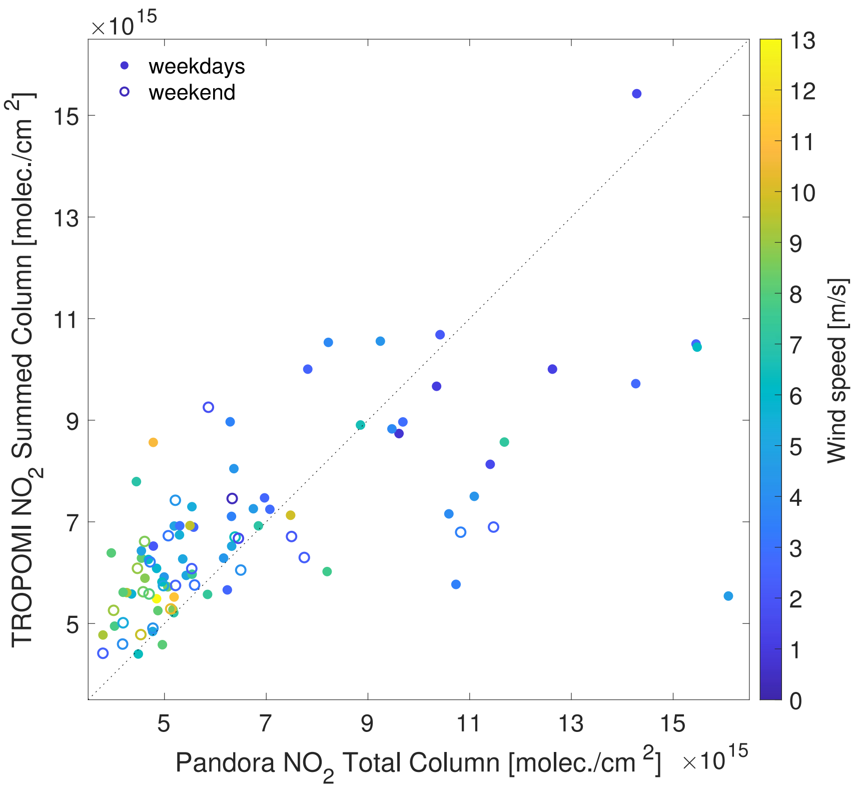

Figure 54 Scatterplot of Pandora and TROPOMI vertical columns. The filled dots correspond to weekdays while the empty circles to the weekends. The colour indicates the wind speed interpolated at the overpass time. The 1 : 1 line is plotted as a dotted line.

4 Outreach

4.1 Scientific publications

- Hakkarainen, J.; Ialongo, I.; Maksyutov, S.; Crisp, D. Analysis of Four Years of Global XCO2 Anomalies as Seen by Orbiting Carbon Observatory-2. Remote Sensing 2019, 11, 850, https://doi.org/10.3390/rs11070850.
- Wang, S., Zhang, Y., Hakkarainen, J., Ju, W., Liu, Y., Jiang, F., and He, W. (2018). Distinguishing anthropogenic CO2 emissions from different energy intensive industrial sources using OCO-2 observations: a case study in northern China. Journal of Geophysical Research: Atmospheres, 123, doi:10.1029/2018JD029005.
- Ialongo, I., Virta, H., Eskes, H., Hovila, J., and Douros, J.: Comparison of TROPOMI/Sentinel 5 Precursor NO2 observations with ground-based measurements in Helsinki, Atmos. Meas. Tech., 13, 205–218, https://doi.org/10.5194/amt-13-205-2020, 2020.
- Duncan, B. N., Ott, L. E., Abshire, J. B., Brucker, L., Carroll, M. L., Carton, J., ... Ialongo, I., et al. (2019). Space-Based Observations for Understanding Changes in the Arctic-Boreal Zone. Reviews of Geophysics, 57. https://doi.org/10.1029/2019RG000652.
- Ialongo I., Fioletov V., McLinden C., Jåfs M., Krotkov N., Li C., Tamminen J., Application of satellite-based sulfur dioxide observations to support the cleantech sector: Detecting emission reduction from copper smelters. Environmental Technology & Innovation, 12, 172-179, https://doi.org/10.1016/j.eti.2018.08.006, 2018.

4.2 Conferences and meetings

- ATMOS 2018, 26-29 November 2018, Saltzburg, AT. Link
- 2019 Living Planet Symposium, 13-17 May 2019, MiCo - Milano Congressi. Milan, Italy. Link
- IG3IS -Transcom workshop and IG3IS science team Meeting, 15 – 18 October 2019, Cité Internationale Universitaire de Paris, France. Link
- Finnish Satellite Workshop and Finnish Remote Sensing Days, 20-22 January 2020, Helsinki, Finland. Link
- IWGGMS 2020, 2-5.6.2020, Webex. Link

4.3 Science communication

The results achieved within the DACES project have been shared via ESA website. A web story including the main results of the project has been published here. Furthermore the results have been shared through social media. Concerning the activities related to societal applications and user engagement, audio and video material and reports have been prepared to reach out and answer to the needs of different users. For example, the results achieved in collaboration with the Finnish clean tech company Outotec have been published among the news in the NASA's website and recognized also by the Millennium Technology Prize on social media. The main results of the project will be also summarized on the FMI website again at the end of the project. We also answered an assignment from the Council of State to monitor air pollution changes during the corona virus crisis.

5 Discussion and future plans

Current CO2 missions have been primarily designed to extend the spatial coverage of the ground-based atmospheric observation networks and to improve the model estimates of biospheric fluxes on regional scale. The COP 21 Paris agreement emphasizes the need to monitor anthropogenic CO2 emissions over a range of scales. The results of DACES project highlight the intrinsic value and capabilities of existing satellite-based CO2 observations for mapping anthropogenic and natural emission patterns, beyond their application as model input information. The concept of XCO2 anomaly is a useful tool to monitor natural and man-made CO2 signatures on global scale. The observed consistency between satellite-based XCO2 anomalies and model outputs (distinguishing fossil fuel and biospheric contributions) demonstrates the capability of satellite observations for describing the CO2 spatio-temporal variability and, in particular, for detecting anthropogenic CO2 emission patterns.

The results achieved during DACES project also highlight the need for satellite observations with high precision, good accuracy and dense sampling covering a wider swath (e.g., few hundred km) than OCO-2, in order to separate individual emission sources (e.g., cities or large power plants) from the background signal. Within the DACES project, we showed how collocated OCO-2 XCO2 data and TROPOMI NO_2 observations (covering a large swath) can be used to identify small-scale anthropogenic CO2 signatures and to calculate CO2 emission from individual sources. In particular, we evaluated several approaches for CO2 plume detection and direct and indirect (via NO2 emission calculation) CO2 emissions estimation based on satellite-based observations.

The methodologies developed during DACES project can also be applied to future XCO_2 missions, such as OCO-3, GOSAT-2, MicroCarb, GeoCarb, and the Chinese and European wide-swath constellations, in particular for the analysis of the observations obtained from the planned European anthropogenic CO2 mission. The global approach can be easily applied to instruments that fly in near-polar, sun-synchronous orbits, however, adjustments to background definition are needed for instruments operating on the International Space Station (e.g., OCO-3) or on geostationary orbit (e.g., GeoCarb) due to the possible influence of diurnal variations and spatial coverage. Further applications of this method could combine anomalies from similar platforms, e.g. belonging to the same constellation.

Finally, one important element of the DACES project is related to the societal applications and user engagement. We collected several user cases in which we demonstrated how satellite-based observations could be used to monitor air pollution in support of decision makers in the public and private sector. We showed how for example local authorities and private companies can make use of satellite observations in verifying emission reductions due to the implementation of environmental policies and clean technology. We also demonstrated how satellite observations of air pollutants can be used in multi-disciplinary studies, e.g. in socio-economic research. Most of these applications utilized satellite observations of short-lived gases as indicator of air pollution or anthropogenic activities in general. Current satellite CO2 observations were not available with the coverage need to analyze many of our case studies. All users expressed their interest in using future satellite CO2 observations with improved coverage and resolution, when available. Further efforts should be made in order to ensure the full exploitation of new satellite-based CO2 observations for societal applications once they become available.

6 Recommendations

In the DACES project we analysed space-based OCO-2 CO2 observations and their connections to the surface fluxes using data-driven methods in both global and local scale. To facilitate this connection, we also utilized other space-based observations such as NO2 and CO retrievals the recently became available from TROPOMI/S5P. The combination of narrow OCO-2 track together with wide-swath of S5P was not ideal, but still provided new insights for monitoring anthropogenic CO2 and for analyzing the future CO2M observations. The key challenge of transforming observational information (e.g., CO2 anomalies given in ppms) to surface fluxes still remains at all scales. This issue requires further developments in both data-driven methods and local-scale atmospheric modeling.

As further developments we recommend the following research topics to be addressed in the future:

1. On global scale: Develop data-driven methodologies based on machine learning techniques to derive information on carbon fluxes training feature vectors of XCO2 anomalies and other space-based observations (current and future datasets, e.g., SIF from TROPOMI/S5P).
2. Extend the anomaly approach to recent missions, such as OCO-3, and the planned European anthropogenic CO2 mission, as well as to different GOSAT CO2 products.
3. On local scale: Further assess and develop emission estimation methods based on satellite-based CO2 observations. Employ more careful atmospheric modeling (e.g., Lagrangian transport and dispersion model) to obtain observation-based NOx-to-CO2 emission ratio to obtain CO2 emission of individual sources. Modeling-based studies are needed to prepare for the exploitation of the observations from the European anthropogenic CO2 mission.
4. User engagement activities: Since most of the users involved in the DACES project expressed their interest in using satellite CO2 observations, further efforts should be made to employ future satellite-based CO2 observations in societal applications. In particular, the improved coverage and resolution of the future CO2M mission is expected to increase the opportunities to employ satellite CO2 observations in societal applications, such as monitoring CO2 emission changes to support decision makers.

7 References

Crisp, D., Pollock, H. R., Rosenberg, R., Chapsky, L., Lee, R. A. M., Oyafuso, F. A., Frankenberg, C., O'Dell, C. W., Bruegge, C. J., Doran, G. B., Eldering, A., Fisher, B. M., Fu, D., Gunson, M. R., Mandrake, L., Osterman, G. B., Schwandner, F. M., Sun, K., Taylor, T. E., Wennberg, P. O., and Wunch, D.: The on-orbit performance of the Orbiting Carbon Observatory-2 (OCO-2) instrument and its radiometrically calibrated products, Atmospheric Measurement Techniques, 10, 59–81, https://doi.org/10.5194/amt-10-59-2017 , 2017.

Fioletov, V. E., McLinden, C. A., Krotkov, N., Moran, M. D., and Yang, K. (2011), Estimation of SO2 emissions using OMI retrievals, Geophys. Res. Lett., 38, L21811, doi:10.1029/2011GL049402.

Fioletov, V. E., McLinden, C. A., Krotkov, N., Li, C., Joiner, J., Theys, N., Carn, S., and Moran, M. D.: A global catalogue of large SO2 sources and emissions derived from the Ozone Monitoring Instrument, Atmospheric Chemistry and Physics, 16, 11 497–11 519, https://www.atmos-chem-phys.net/16/11497/2016/ , 2016.

Hakkarainen, J., Ialongo, I., and Tamminen, J.: Direct space-based observations of anthropogenic CO2 emission areas from OCO-2, Geophysical Research Letters, 43, 11,400– 11,406, https://doi.org/10.1002/2016GL070885 , 2016.

Hakkarainen, J.; Ialongo, I.; Maksyutov, S.; Crisp, D. Analysis of Four Years of Global XCO2 Anomalies as Seen by Orbiting Carbon Observatory-2. Remote Sensing 2019, 11, 850, https://doi.org/10.3390/rs11070850 .

Wang, S., Zhang, Y., Hakkarainen, J., Ju, W., Liu, Y., Jiang, F., and He, W. (2018). Distinguishing anthropogenic CO2 emissions from different energy intensive industrial sources using OCO-2 observations: a case study in northern China. Journal of Geophysical Research: Atmospheres, 123, doi:10.1029/2018JD029005.

Ialongo, I., Virta, H., Eskes, H., Hovila, J., and Douros, J.: Comparison of TROPOMI/Sentinel 5 Precursor NO2 observations with ground-based measurements in Helsinki, Atmos. Meas. Tech., 13, 205–218, https://doi.org/10.5194/amt-13-205-2020 , 2020.

Duncan, B. N., Ott, L. E., Abshire, J. B., Brucker, L., Carroll, M. L., Carton, J., ... Ialongo, I., et al. (2019). Space-Based Observations for Understanding Changes in the Arctic-Boreal Zone. Reviews of Geophysics, 57. https://doi.org/10.1029/2019RG000652.

Ialongo I., Fioletov V., McLinden C., Jåfs M., Krotkov N., Li C., Tamminen J., Application of satellite-based sulfur dioxide observations to support the cleantech sector: Detecting emission reduction from copper smelters. Environmental Technology & Innovation, 12, 172-179, https://doi.org/10.1016/j.eti.2018.08.006 , 2018.

Nassar, R., Hill, T. G., McLinden, C. A., Wunch, D., Jones, D. B. A., and Crisp, D.: Quantifying CO2 Emissions From Individual Power Plants From Space, Geophysical Research Letters, 44, 10,045–10,053, https://doi.org/10.1002/2017GL074702 , 2017.

Oda, T., Maksyutov, S., and Andres, R. J.: The Open-source Data Inventory for Anthropogenic CO2, version 2016 (ODIAC2016): a global monthly fossil fuel CO2 gridded emissions data product for tracer transport simulations and surface flux inversions, Earth System Science Data, 10, 87–107, https://doi.org/10.5194/essd-10-87-2018 , 2018.

Outotec: Sustainability Report 2017, available at: http://www.outotec.com/globalassets/sustainability-report/2017/outotec_sr_2017_final_23032018.pdf , pp 35, 2018.

Neste: Sustainability Report 2018, available at: http://www.neste.com/sustainabilityreport , pp 49, 2019.

Reuter, M., Buchwitz, M., Hilboll, A., Richter, A., Schneising, O., Hilker, M., Heymann, J., Bovensmann, H., and Burrows, J. P.: Decreasing emissions of NOx relative to CO2 in East Asia inferred from satellite observations, Nature Geoscience, 7, 792 EP –, https://doi.org/10.1038/ngeo2257 , 2014.

Schwandner, F. M., Gunson, M. R., Miller, C. E., Carn, S. A., Eldering, A., Krings, T., Verhulst, K. R., Schimel, D. S., Nguyen,
H. M., Crisp, D., O'Dell, C. W., Osterman, G. B., Iraci, L. T., and Podolske, J. R.: Spaceborne detection of localized carbon dioxide sources, Science, 358, https://doi.org/10.1126/science.aam5782 , 2017.

Wunch, D., Wennberg, P. O., Osterman, G., Fisher, B., Naylor, B., Roehl, C. M., O'Dell, C., Mandrake, L., Viatte, C., Kiel, M., Griffith, D. W. T., Deutscher, N. M., Velazco, V. A., Notholt, J., Warneke, T., Petri, C., De Maziere, M., Sha, M. K., Sussmann, R., Rettinger, M., Pollard, D., Robinson, J., Morino, I., Uchino, O., Hase, F., Blumenstock, T., Feist, D. G., Arnold, S. G., Strong, K., Mendonca, J., Kivi, R., Heikkinen, P., Iraci, L., Podolske, J., Hillyard, P. W., Kawakami, S., Dubey, M. K., Parker, H. A., Sepulveda, E., García, O. E., Te, Y., Jeseck, P., Gunson, M. R., Crisp, D., and Eldering, A.: Comparisons of the Orbiting Carbon Observatory-2 (OCO-2) XCO2 measurements with TCCON, Atmospheric Measurement Techniques, 10, 2209–2238, https://doi.org/10.5194/amt-10-2209-2017 , 2017.